J. Fluid Mech. (1969), *vol.* 38, *part* 3, *pp.* 577–612
Printed in Great Britain

Some measurements in the self-preserving jet

By I. WYGNANSKI AND H. FIEDLER
Boeing Scientific Research Laboratories, Seattle, Washington 98124

(Received 6 June 1968 and in revised form 12 March 1969)

The axisymmetric turbulent incompressible and isothermal jet was investigated by use of linearized constant-temperature hot-wire anemometers. It was established that the jet was truly self-preserving some 70 diameters downstream of the nozzle and most of the measurements were made in excess of this distance. The quantities measured include mean velocity, turbulence stresses, intermittency, skewness and flatness factors, correlations, scales, low-frequency spectra and convection velocity. The r.m.s. values of the various velocity fluctuations differ from those measured previously as a result of lack of self-preservation and insufficient frequency range in the instrumentation of the previous investigations. It appears that Taylor's hypothesis is not applicable to this flow, but the use of convection velocity of the appropriate scale for the transformation from temporal to spatial quantities appears appropriate. The energy balance was calculated from the various measured quantities and the result is quite different from the recent measurements of Sami (1967), which were obtained twenty diameters downstream from the nozzle. In light of these measurements some previous hypotheses about the turbulent structure and the transport phenomena are discussed. Some of the quantities were obtained by two or more different methods, and their relative merits and accuracy are assessed.

1. Introduction

The present paper is concerned with an experimental investigation of the self-preserving turbulent axisymmetric jet. This, being a relatively simple turbulent shear flow, has been investigated in some detail before. Many of the mean velocity measurements with Pitot tubes are well summarized in Hinze (1959). Most of the turbulent quantities in the fully developed jet are associated with Corrsin (1943), Corrsin & Uberoi (1949, 1951), and Corrsin & Kistler (1955).

Existing measurements of mean velocity distributions indicate that the profile becomes reasonably self-preserving some few diameters downstream of the nozzle, although most of these results exhibit a considerable scatter at the edges of the flow. The turbulent intensities, however, show marked departures from self-preservation even on the axis of the jet. It was concluded by Townsend (1956) that the effect of the initial conditions near the nozzle exit diminishes rather slowly with downstream distance, and the reported measurements were not made far enough downstream to attain self-preservation. The lack of self-preservation handicapped the study of this flow, and did not enable a proper comparison with other self-preserving flows.

The local turbulence levels at the edges of jet flows are high, making the measurements extremely difficult. Indeed, all the older measurements were adversely affected by this fact, since the hot-wire output did not respond linearly to the instantaneous velocity. In order to avoid some of the experimental difficulties, it was suggested (Townsend 1956) that measurements were made in a high-velocity jet discharging into a low-velocity stream. This suggestion was taken up by Bradbury (1965) in the two-dimensional jet flow. However, since a jet in a uniform stream is inherently non-self-preserving, one may be replacing one difficulty by another.

Consequently, it was felt that accurate measurements in the self-preserving jet could be accomplished by using linearized constant-temperature hot-wire anemometers and integrating over long periods of time to obtain good statistical averages also in the outer region of the flow. The distributions of mean velocities and turbulent intensities, as well as higher-order velocity products across the jet, indicate that the self-preserving region was attained. The investigation was then expanded to include double and triple velocity products, intermittency, energy balance, space–time correlations and scales, convection velocity and its dependence on frequency.

The experiment was carried out at air speeds allowing the flow to be considered incompressible. (The velocity at the jet nozzle was in most cases 51 m/sec, but some measurements were made at 72 m/sec.) The Reynolds number based on nozzle diameter was of the order of 10^5.

2. Experimental equipment and procedure

The jet emerged from a nozzle 1·04 in. in diameter at a Reynolds number of 10^5. The velocity of the jet was maintained constant to an accuracy better than 1 %, and the temperature was maintained constant to within 1 °F. The room is air-conditioned and the temporal variation of temperature in it did not exceed 2 °F. The air was cleaned using a Honeywell electrostatic precipitator, which removed particles and hydrocarbons in the air down to 0·04 microns in diameter. At the exit plane the jet was essentially laminar, having a turbulence intensity of approximately 0·1 %. The nozzle was placed in the middle of a wall $7\frac{1}{2}$ ft. high and 8 ft. wide and the entire jet was enclosed in a cage ($7\frac{1}{2}$ ft. high, 8 ft. wide, 17 ft. long and open on the far side) made out of two $\frac{1}{16}$ in. mesh screens placed $2\frac{1}{2}$ in. apart. This arrangement eliminated all room draughts without altering the flow, and thus permitted measurements far downstream from the nozzle.

Constant-temperature DISA anemometers and linearizers were used with standard DISA hot wires (1·2 mm long and 5 μm in diameter). For measurements of turbulent intensities a.c. capacitive couplings were constructed and checked to have a flat response to frequencies of 0·05 Hz. The squared a.c. signals were integrated by using operational amplifiers in conjunction with capacitors. The integrated voltage was read on a Hewlett Packard digital voltmeter, and the time was recorded on the same company's counter. Sometimes, three integrators were used simultaneously (e.g. correlation measurements), while the signals were processed in different ways; this procedure reduced the scatter significantly.

The integration times were increased until the scatter in the r.m.s. value was less than 1 %; integration times of 5 min were not uncommon. Various Philbrick analogue elements† were used for squaring, multiplying, adding and subtracting of the signals. Tektronix differentiating circuits were used for differentiation with respect to time. The autocorrelations were measured with a P.A.R.-100 correlator, and the harmonic analysis was performed with Krohn–Hite band pass filters. When x-probes were used, each of the attenuators on the linearizers was adjusted to give the same output for each wire when the probe was perfectly aligned with the stream; the yaw sensitivity of each wire was then checked. The entire network was calibrated before each run and rechecked at the end of a run.

The turbulent intensities were corrected for tangential cooling according to the formulas given by Champagne & Sleicher (1967). The response of the hot wire was assumed linear, and no corrections resulting from higher-order terms were applied. The higher-order terms were measured, however, and are given in the report.

3. The mean velocity

The mean velocity was measured with a single hot wire perpendicular to the axis of the flow. After determining that the jet was indeed axisymmetric, the traverses were made along one radius only. Figure 1 shows the mean velocity distribution across the jet at different stations downstream, ranging from 40 to 100 diameters. The velocity scale in this figure is the maximum velocity at each section, and the distance from the axis of symmetry, y, is divided by the distance from the nozzle. Quite often the length chosen to render y dimensionless is the local half-width of the profile, namely the width corresponding to the point where the mean velocity is equal to one-half of its value on the axis. The use of this definition does not show any changes in the location of the hypothetical origin of the flow, which are sometimes significant (e.g. in the small-deficit wake, Townsend 1956); and deviations from similarity are less visible. From figure 1 it may be deduced that the mean velocity profile is similar, and the hypothetical origin does not change with x. The measured values agree quite well with those reported by Hinze & Van der Hegge Zijnen (1949), but the scatter at large values of y/x was eliminated by averaging the measurements over a long period of time.

Two theoretical models for predicting the shape of the mean velocity profile exist. One, based on the mixing-length hypothesis, was obtained by Tollmien (1926), and another, based on the assumption of constant eddy exchange coefficient across the flow, was calculated by Schlichting (1961). Neither of these two predicted profiles agrees well with the experimental values across the entire flow. Tollmien's solution agrees moderately well with experiment in the outer part of the flow, while the solution of Schlichting is in good agreement with measured values in the inner part of the flow (figure 2). The concept of eddy viscosity applies only to turbulent flow (Townsend 1949), yet most measurements

† Model P65AU (with a minimum large-signal frequency response of 20 kHz), models PSQP and PSQN.

performed in turbulent free shear flows represent a time average of velocity inside and outside the turbulent front. To enable a proper comparison between theory and experiment, separate measurements should be made in the rotational and irrotational regions as shown recently by Kibens & Kovasznay (1967) in turbulent boundary layers. Assuming that the entrainment velocity outside the

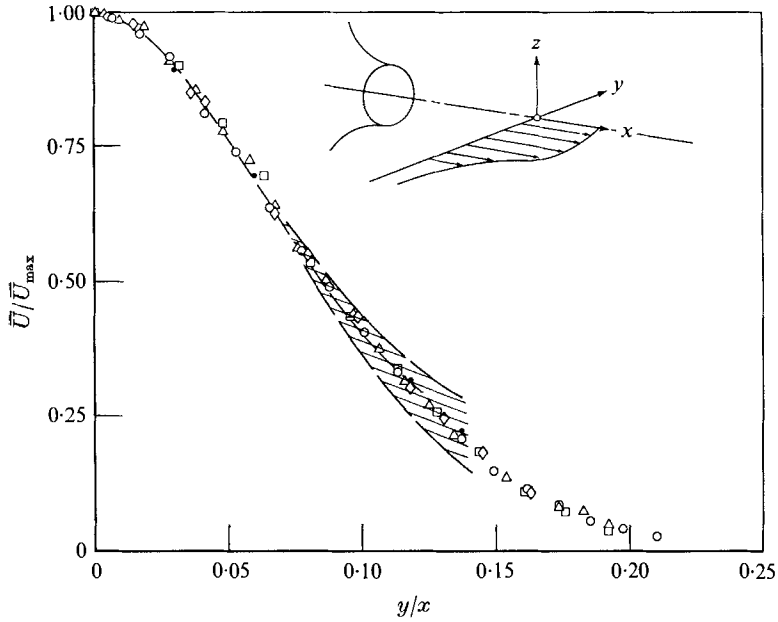

FIGURE 1. Mean velocity profile. — — —, Hinze *et al.* (1949). ○, x/D = 40; △, 50; □, 60; ◇, 75; ●, 97·5.

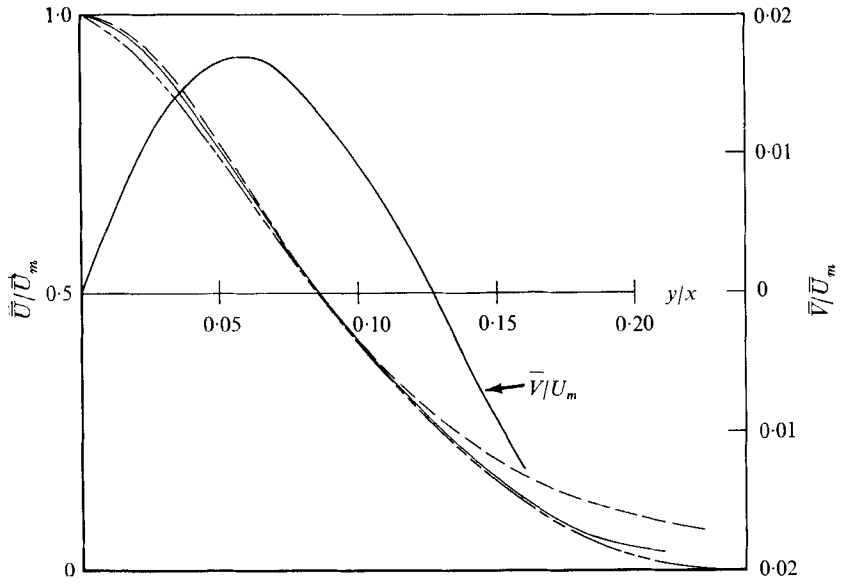

FIGURE 2. Mean velocities: comparison with theories. ——, experimental values; — — —, Schlichting (1961), and — · · —, Tollmien (1926), theory.

turbulent front is primarily normal to the jet axis (Stewart 1956), the mean velocity profile in the turbulent region is obtained by dividing the overall time average by the intermittency factor, γ. In this case, the theoretical profile of Schlichting underestimates the experimental values of $\overline{U}/\gamma$ (see figure 2). Since the entrainment velocity of the irrotational fluid in the vicinity of the turbulent front has also a component parallel to the jet axis,the value of $\overline{U}/\gamma > U_{\text{turbulent}}$; this may explain the discrepancy between theory and experiment. The transverse velocity $\overline{V}$ given in figure 2 was calculated using the continuity equation.

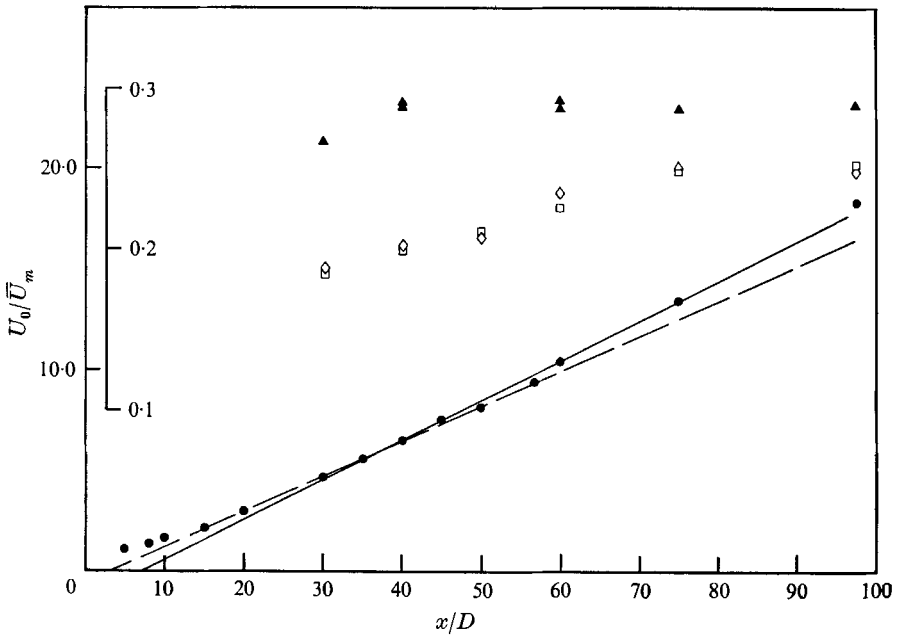

FIGURE 3. Variation of mean velocity and turbulent intensities along the jet centre-line. ●, $U_0/\overline{U}_m$; ▲, $\sqrt{(\overline{u'^2})}/\overline{U}_m$); □, $\sqrt{(\overline{v'^2})}/\overline{U}_m$; ◇, $\sqrt{(\overline{w'^2})}/\overline{U}_m$).

The variation of the mean velocity along the axis of the jet is given in figure 3. Judging from the mean velocity alone, it would appear that the jet is already self-preserving at some 20 nozzle diameters downstream of the nozzle. If the measurements were concluded at $x/D \leqslant 50$ the hypothetical origin of the flow would appear to be located 3 diameters in front of the nozzle. Taking into account measurements at $x/D > 50$, the hypothetical origin was moved to 7 diameters in front of the nozzle. A similar observation was made by Townsend (1956) for the small-deficit wake, and it may be concluded that the rate of growth of the jet is sensitive to conditions of self-preservation, while the shape of the normalized velocity profile is not.

4. Turbulent intensities

The turbulent intensities were measured with an X meter, but the r.m.s. values of the longitudinal fluctuations were also obtained with a single normal wire and the results were identical. The response of the hot wire was assumed

linear, and the direction of the mean flow parallel to the axis of the jet. The variation of the turbulence intensities along the axis of the jet is plotted in figure 3. It is interesting to note that, whereas the longitudinal fluctuations become self-similar some 40 diameters downstream of the nozzle, the radial and tangential turbulence intensities attain similarity some 70 diameters from the nozzle. It is only then that the flow becomes truly self-preserving. A given body of fluid is

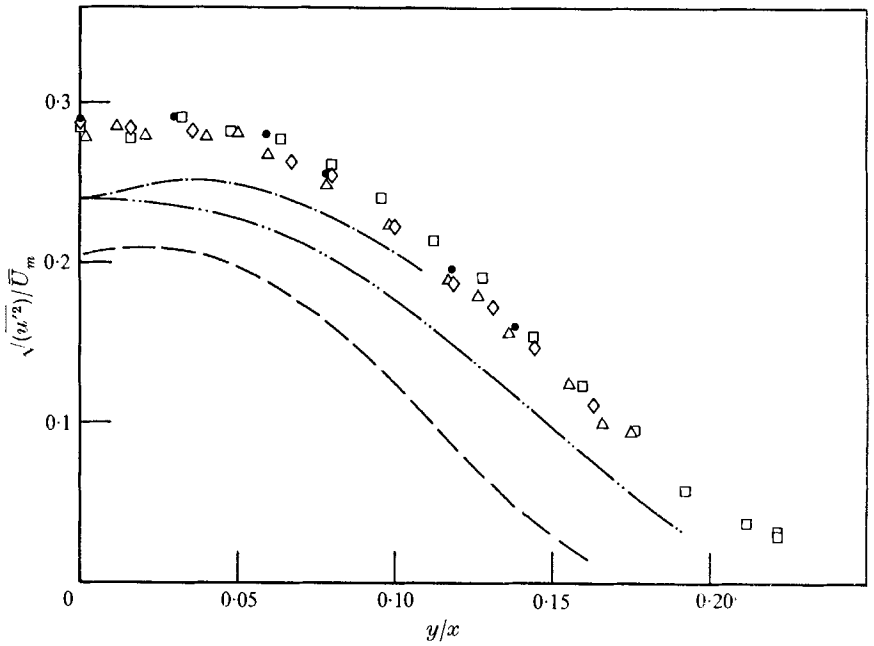

FIGURE 4. Intensity of u'-fluctuation across the jet. — —, Corrsin (1949), $x/d = 20$; — · —, present investigation, $x/d = 20$; — · · —, present investigation, $x/d = 60$, using DISA correlator (flat frequency down to 5 Hz). △, $x/d = 50$; □, 60; ◇, 75; ●, 97·5.

said to be in a self-preserving state when all of its turbulent components are in equilibrium. However, since the energy is transferred from the mean motion directly to u' fluctuations, and only pressure-velocity-gradient correlations transfer the energy further to other components of the turbulent motion, it is little wonder that similarity is reached in steps. First, the mean velocity becomes similar, which leads to certain production of u', and only after a balance is reached between these two quantities an equilibrium may be attained in the transverse components as well. Townsend (1956) predicted that self-preserving flow may be realized only some 50 diameters downstream of the nozzle. The present results verify this statement.

The magnitude of $\overline{v'^2}$ and $\overline{w'^2}$ is less than that of $\overline{u'^2}$ even as far downstream as 100 diameters. This result does not agree with measurements of Gibson (1963), who observed almost a perfect isotropy on the centre-line of the jet at $x/D = 50$. This discrepancy would have been even greater if our measured values of the transverse velocity fluctuations were not corrected for tangential cooling. The value of $\overline{u'^2}$ measured on the jet axis is, however, in agreement with Gibson's data.

The radial distribution of the various turbulence intensities as well as of the shear stress are shown in figures 4–7.

In figure 4 a comparison is made between the present measurements and those of Corrsin & Uberoi (1949); and the results differ by some 25 %. This discrepancy is attributed to two factors: (i) at $x/D = 20$ the flow did not attain its self-preserving state, and the relative turbulent intensity is thus significantly lower; (ii) the frequency response of the equipment used by Corrsin was not tested for frequencies below 7 Hz. A significant percentage of the turbulent intensity is, however, present at frequencies below 7 Hz. When $\overline{u'^2}$ was measured at

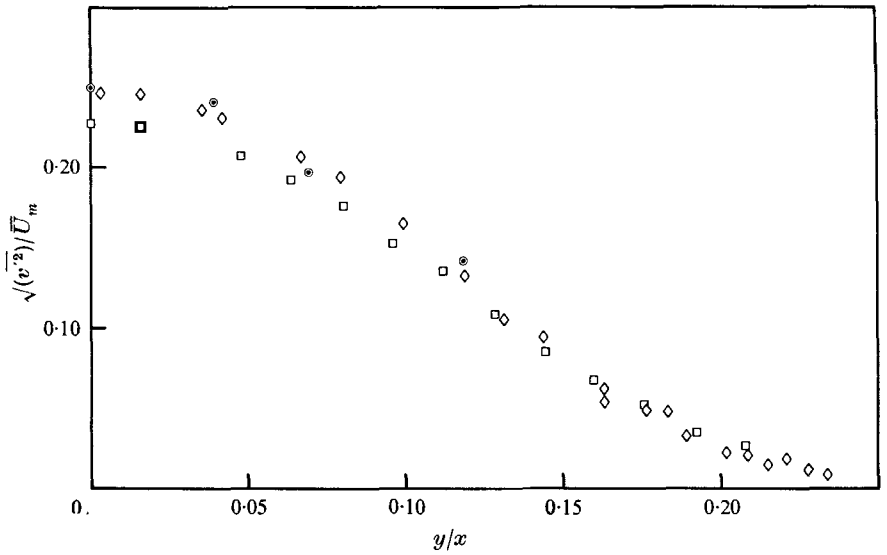

FIGURE 5. Intensity of v'-fluctuation across the jet. □, $x/D = 60$; ◇, 75; ⊙, 97·5.

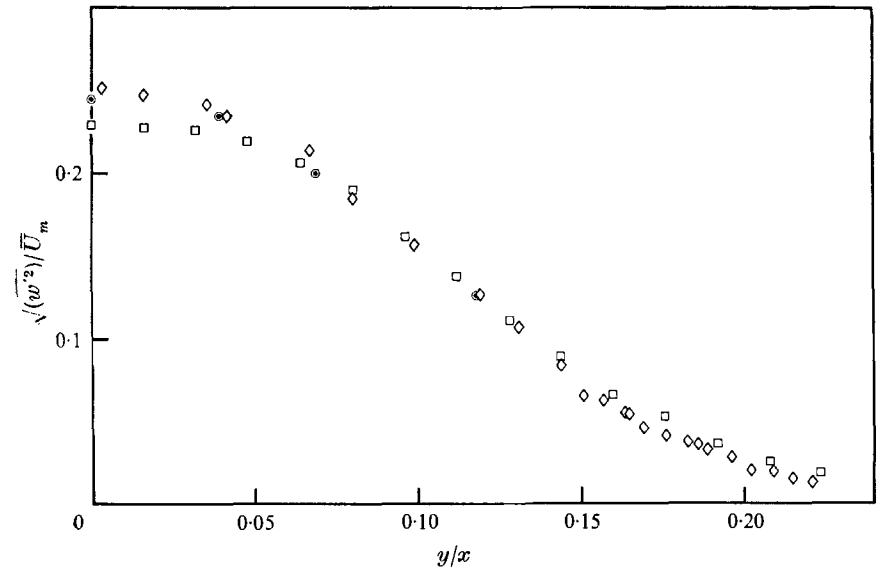

FIGURE 6. Intensity of w'-fluctuation across the jet.
□, $x/D = 60$; ◇, 75; ⊙, 97·5.

$x/D = 60$ using the standard DISA correlator, which has a flat response to 5 Hz, the resulting curve was significantly lower (figure 4). Spectral analyses of u' and v' were undertaken at $x/D = 90$, and the results are plotted in figure 8. At that position in the jet, the filtering of all frequencies below 2 Hz may introduce an error of 27 % in $\overline{u'^2}$, and about 11 % in $\overline{v'^2}$. The fact that the longitudinal intensity contains more of its energy at the lower part of the spectrum is indicative of the manner in which the energy is being transferred, namely from the mean motion to $\overline{u'^2}$, and then to $\overline{v'^2}$ and $\overline{w'^2}$.

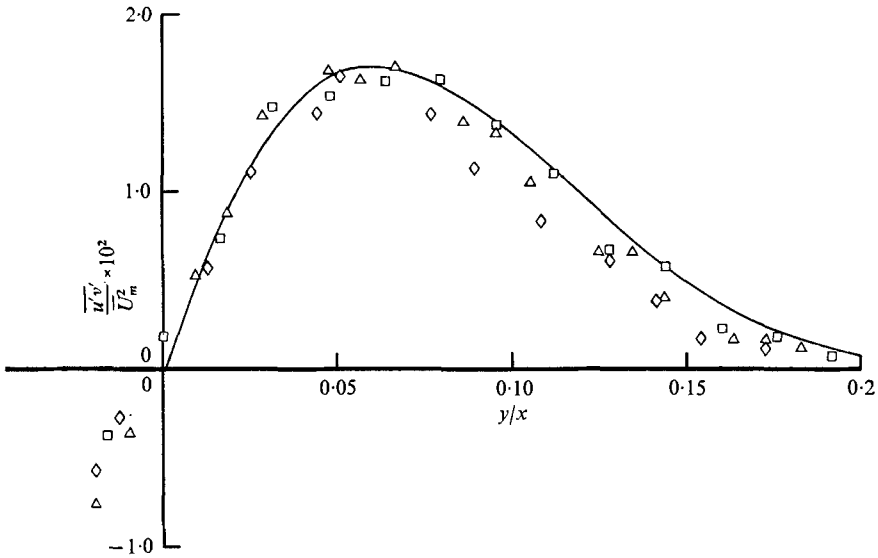

FIGURE 7. Shear stress distribution across the jet. ——, calculated from mean velocity profile. △, $x/D = 50$; □, 60; ◇, 75.

Towards the edge of the jet ($y/x > 0{\cdot}2$), the intermittency factor is small, and the intensity of the lateral fluctuations should be larger than the intensity of the longitudinal fluctuations (Phillips 1955). From comparison of figure 4 with figures 5 and 6, a conflicting conclusion may be drawn. However, the interpretation of the experimental results at large y/x is not reliable, because the direction of the mean flow in that region is not known. This anomaly may be explained in the following manner. From the distribution of intermittency (figure 9), an estimate of the mean velocity profiles inside the turbulent flow was obtained. With the use of continuity, the angle between the direction of the mean flow and the axis of the X wire was calculated, and it appears that this angle was less than 3°. It may thus be assumed that, inside the turbulent front, the hot wire was perfectly aligned with the mean flow. Outside the turbulent front the entrainment velocity is approximately normal to the axis of the jet (Stewart 1956); and thus, from the cosine law, the following equations apply:

$$\overline{u'^2}_{\text{measured}} \approx \overline{u'^2}_{\text{turb}}\gamma + \overline{v'^2}_{\text{pot}}(1-\gamma),$$
$$\overline{v'^2}_{\text{measured}} \approx \overline{v'^2}_{\text{turb}}\gamma + \overline{u'^2}_{\text{pot}}(1-\gamma),$$
$$\overline{w'^2}_{\text{measured}} \approx \overline{w'^2}_{\text{turb}}\gamma + \overline{w'^2}_{\text{pot}}(1-\gamma),$$

where γ is the intermittency, and only the linear response of the hot wire is considered.

The potential fluctuations may be estimated from the above equations when $\gamma \to 0$. For $y/x = 0{\cdot}22$,

$$\frac{\overline{v'^2_{\text{pot}}}}{U_m^2} \approx 7{\cdot}8 \times 10^{-6}, \quad \frac{\overline{u'^2_{\text{pot}}}}{U_m^2} = \frac{\overline{w'^2_{\text{pot}}}}{U_m^2} \approx 3{\cdot}7 \times 10^{-6};$$

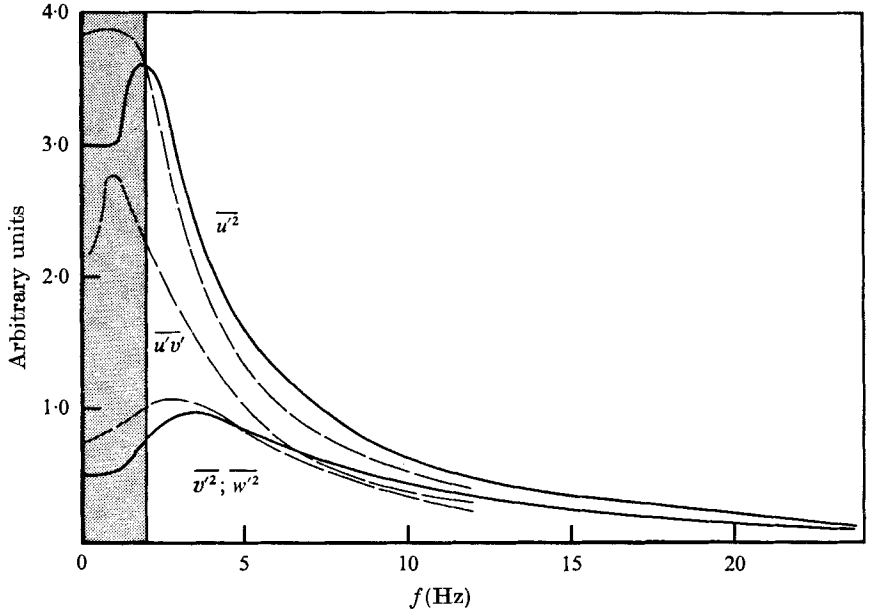

FIGURE 8. Power spectral densities of u', v' and $u'v'$ at $x/D = 90$. Error due to 2 Hz clipping: for $\overline{u'^2}$, $\sim$ 27 %; for $\overline{v'^2}$, $\sim$ 11 %. – – –, location of highest shears; ——, on axis.

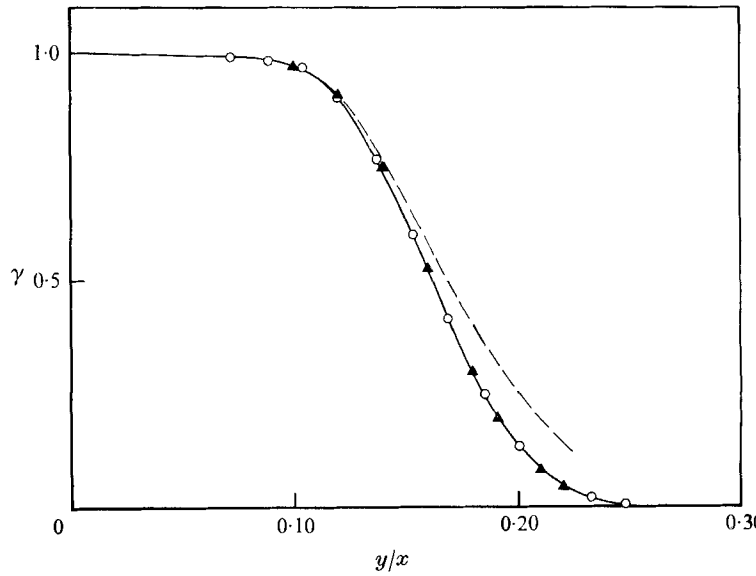

FIGURE 9. Distribution of the intermittency factor across the jet. — — —, from flatness-factor of u'; ——, counting method; ▲, Corrsin & Kistler (1955).

and hence there is no conflict with the theoretical results of Phillips (1955) namely

$$\overline{v'^2_{\text{pot}}} = \overline{u'^2_{\text{pot}}} + \overline{w'^2_{\text{pot}}}.$$

These results can serve only as an order-of-magnitude estimate. The distribution of $\overline{u'v'}$ (figure 7) appears to be narrower than the distribution of the normal

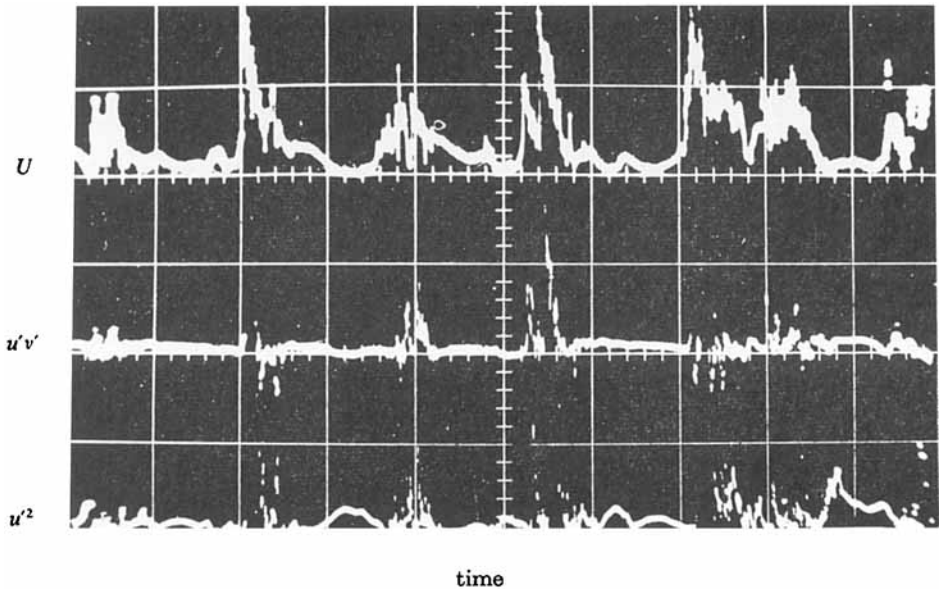

FIGURE 10. Simultaneous oscilloscope traces of U, u'^2 and $u'v'$ signal.

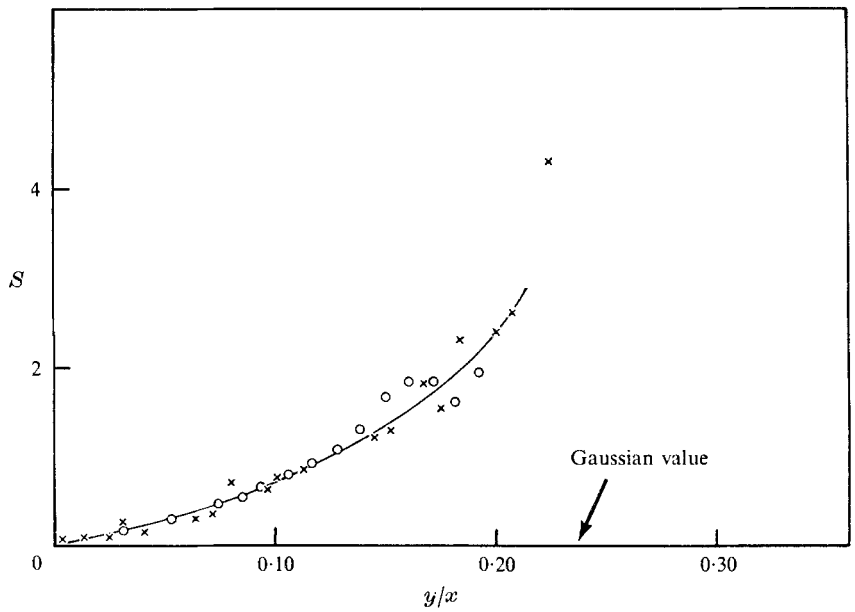

FIGURE 11. Variation of skewness factor across the jet. ×, u'; ○, v'.

fluctuations. This may imply that the magnitude of the shear stress outside the turbulent front is vanishingly small. To check this contention, photographs of u'^2, U and $u'v'$ were taken, and are shown in figure 10. The turbulent bursts passing the hot wires are distinguishable by their high frequency; the potential fluctuations are visible in the trace of U and u'^2; but the trace of $u'v'$ outside the turbulent bursts appears quite steady.

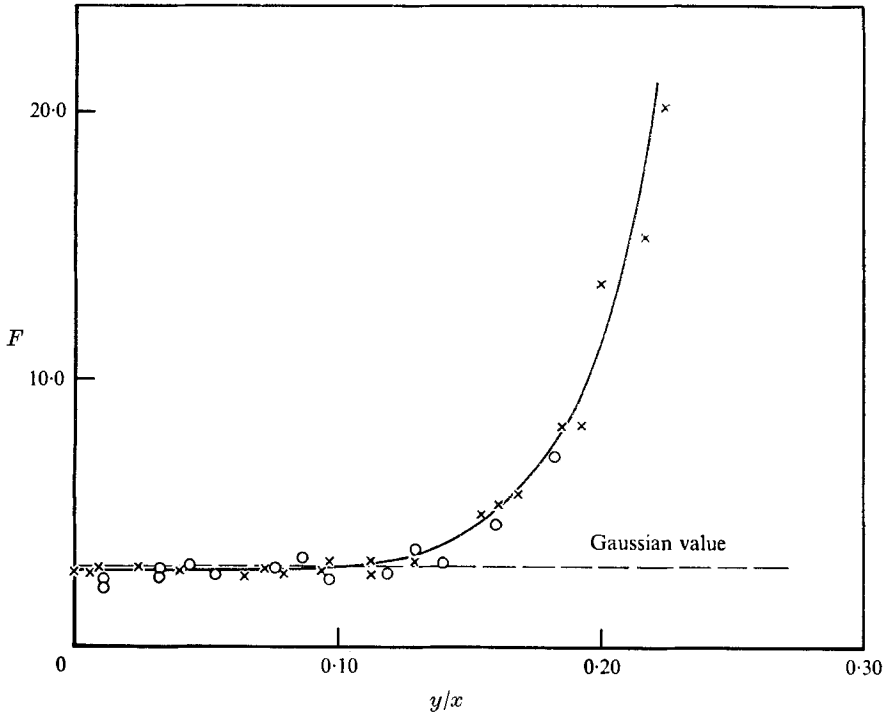

FIGURE 12. Variation of flatness factor across the jet. ×, u'; ○, w'.

The distribution of $\overline{u'v'}$ was also calculated from the mean velocity profile, neglecting the normal stress term $(\partial/\partial x)(\overline{u'^2}-\overline{v'^2})$, and it is plotted in figure 7. The good agreement between the calculated and the measured profile of $\overline{u'v'}$ is attributed in part to the small scatter in the mean velocity distribution.

5. Intermittency, skewness and flatness factors

The intermittency was measured using $\partial u/\partial t$ and $\partial^2 u/\partial t^2$ as the basic signal, and so the potential fluctuations, which contain only low frequencies, were eliminated. The signal was processed by the method of Heskestad (1963) and by a method suggested by Bradbury (1964). The triggering level was adjusted before each reading and checked against traces of oscilloscope photographs. The two methods of measurement agreed very well. It became apparent that for $x/D > 20$ single differentiation sufficed. The measurements are in perfect agree-

ment with those of Corrsin & Kistler (1955) as indicated in figure 9. Townsend (1949) suggested that the flatness factor of any velocity fluctuation can be used as a measure of intermittency. In figure 9, the ratio

$$[\overline{u'^4}/(\overline{u'^2})^2]_{CL}/[\overline{u'^4}/(\overline{u'^2})^2]$$

is given, and it appears that it deviates from the measured intermittency distribution. Deviation in the same direction was observed by Heskestad (1963) in the two-dimensional jet and it results from $(\overline{u'^2})_{\text{pot}} > 0$.

The skewness factors of u' and v' are given in figure 11 and the flatness factors of u' and w' are given in figure 12. It appears that the deviation of the probability density distribution from a Gaussian curve is approximately the same for all components, at least up to the fourth moment.

6. Correlations and integral scales

The variation of the longitudinal correlation coefficient

$$R_{11} = \frac{\overline{u'(x+\frac{1}{2}\Delta x)\,u'(x-\frac{1}{2}\Delta x)}}{[\overline{u'^2(x+\frac{1}{2}\Delta x)}]^{\frac{1}{2}}\,[\overline{u'^2(x-\frac{1}{2}\Delta x)}]^{\frac{1}{2}}}$$

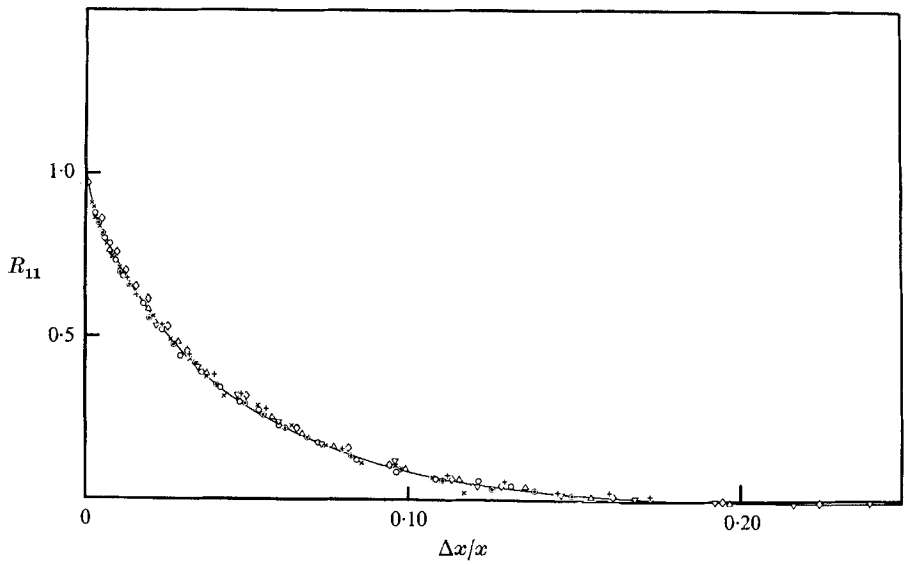

FIGURE 13. Longitudinal correlation on the jet centre-line. ×, $x/D = 90$; ○, 80; ⊙, 70; +, 60; △, 50; ▽, 40; ◇, 30. $\Lambda_f = 0{\cdot}0385x$.

along the centre-line of the jet is given in figure 13. It appears that the structure of the eddies is self-preserving from $x/D > 40$, at $x/D = 30$ slight deviation from self-preservation may be observed, particularly in the small-scale motion (i.e. $\Delta x \to 0$). The variation of R_{11} with y is given in figure 14; the increasing scatter in the experimental results with increase of y/x is attributed to the intermittency.

The associated integral scale Λ_f is shown on these figures. At a given cross-section Λ_f increases in the lateral direction and at $y/x = 0{\cdot}2$ it is almost double in comparison with Λ_f on the axis. The distribution of the lateral correlation

$$R_{12} = \frac{\overline{u'(y+\frac{1}{2}\Delta y)\,u'(y-\frac{1}{2}\Delta y)}}{[\overline{u'^2(y+\frac{1}{2}\Delta y)}]^{\frac{1}{2}}\,[\overline{u'^2(y-\frac{1}{2}\Delta y)}]^{\frac{1}{2}}}$$

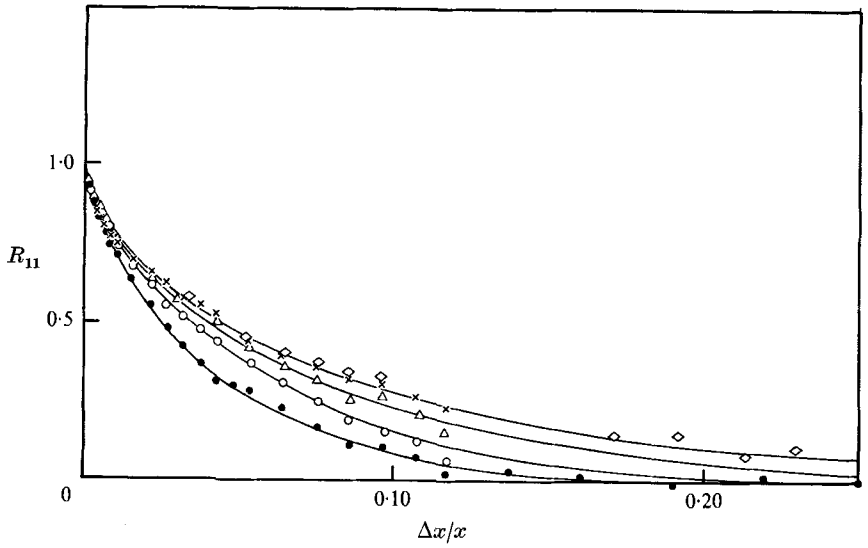

FIGURE 14. Variation of the longitudinal correlation across the jet. ●, $\Lambda_f \approx 0{\cdot}0385x$, $y/x = 0$; ○, $0{\cdot}0512x$, 0·05; △, $0{\cdot}0623x$, 0·10; ×, $0{\cdot}073x$, 0·15; ◇, $0{\cdot}0735x$, 0·20.

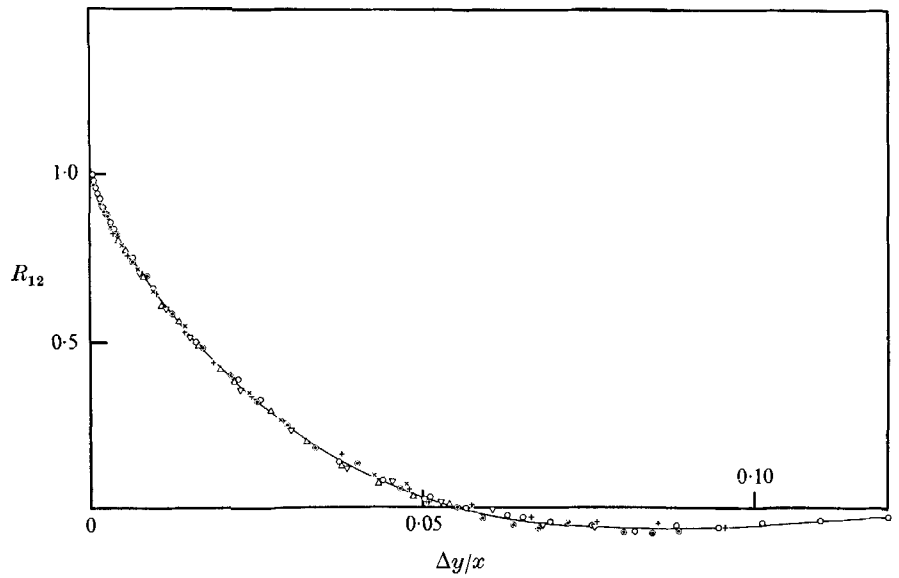

FIGURE 15. Lateral correlation on the jet centre-line, ○, $x/D = 60$; ⊙, 90; △, 70; ×, 80; ▽, 50; +, 40. $\Lambda_g = 0{\cdot}0157x$.

is given in figures 15 and 16 and the lateral distributions of the scales Λ_f and Λ_g are given in figure 17. The behaviour of R_{12} with Δy on the axis of the jet is different from the variation of R_{11} with separation distance, namely $R_{12} < 0$ for $\Delta y/x > 0{\cdot}05$. This would indicate the existence of some periodicity near the

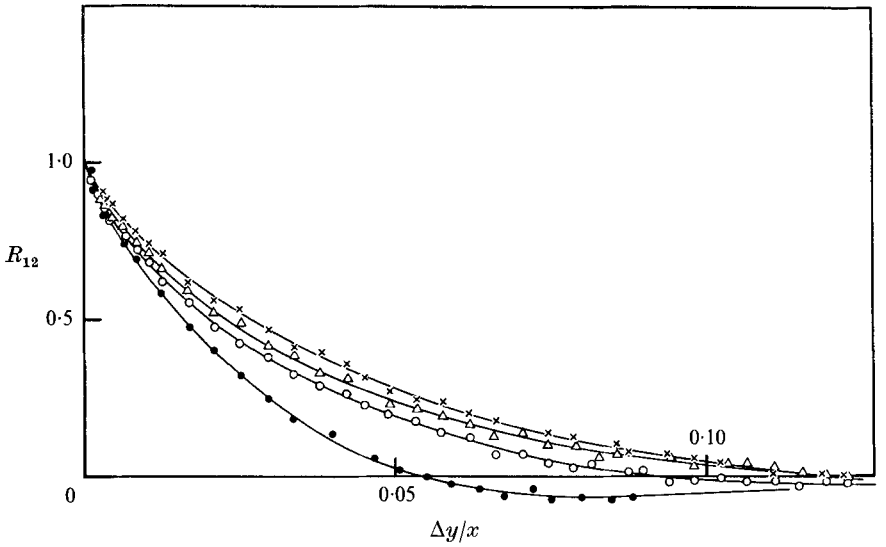

FIGURE 16. Variation of the lateral correlation across the jet. ●, $\Lambda_g \approx 0{\cdot}0157x$, $y/x = 0$; ○, $0{\cdot}0225x$, 0·05; △, $0{\cdot}0280x$, 0·10; ×, $0{\cdot}0300x$, 0·15.

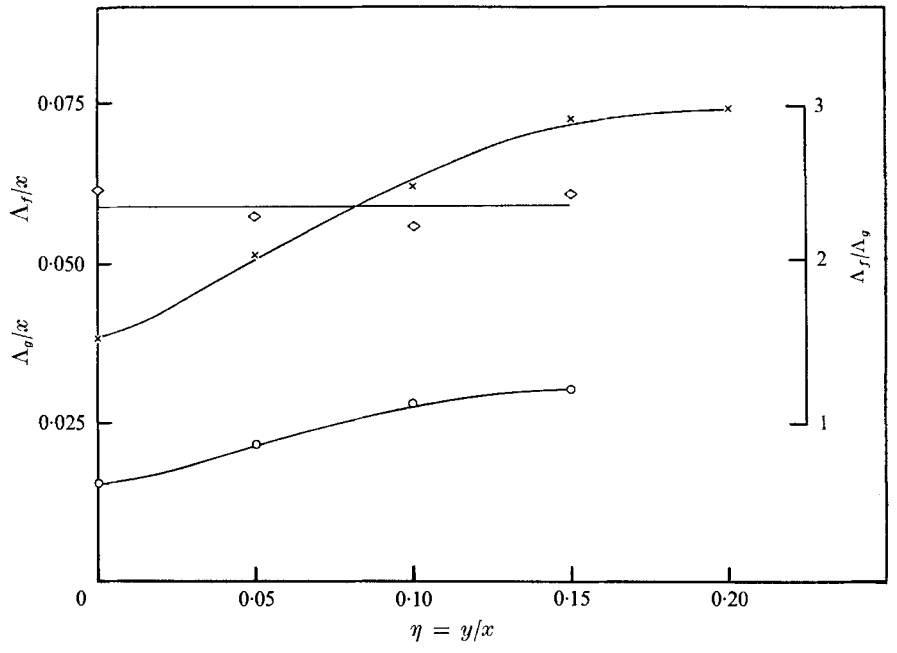

FIGURE 17. Distribution of integral scales across the jet. ◇, Λ_f/Λ_g; ×, Λ_f; ○, Λ_g.

centre-line of the jet. With the increase of the lateral distance from the axis the negative dip in R_{12} becomes less apparent. The integral scale Λ_g increases with y at a given cross-section and the ratio of Λ_f/Λ_g is approximately a constant ($\Lambda_f/\Lambda_g \approx 2{\cdot}3$). Correlations were measured by a number of investigators, and some of the results are presented in table 1.

Author	$\frac{x}{D}$	$\frac{y}{x}$	$\frac{\Lambda_f}{x}$	$\frac{\Lambda_g}{x}$	$\frac{\Lambda_f}{\Lambda_g}$	$\frac{y}{x}$	$\frac{\Lambda_f}{x}$	$\frac{\Lambda_g}{x}$	$\frac{\Lambda_f}{\Lambda_g}$
Corrsin & Uberoi (1949)	20	0	0·071	0·0132	5·37	—	—	—	
Laurence (1956)	20	0	0·018	—	—	0·1	0·01	—	—
Gibson (1963)	50	0	0·081	—	—	0·04	0·081	—	—
Sami (1967)	10	—	—	—	—	0·1	0·085	0·065	1·31
Present investigation	90	0	0·0385	0·0157	2·43	0·1	0·062	0·028	2·21

TABLE 1

From a closer examination of the work of Laurence (1956), Sami (1967) and Davies *et al.* (1963), it appears that in the mixing region the integral scales increase rapidly with x. Further downstream, after the disappearance of the potential core, the scales no longer increase with the downstream distance, but may even decrease. In the self-preserving region the scales are again proportional to x, but the proportionality constant is smaller than that in the mixing region. The lateral scale measured by Corrsin & Uberoi (1951) was obtained in the same manner as in the present investigation and the agreement between the two is fairly good in spite of the difference in x/D. The longitudinal scales, however, were obtained by Corrsin (1943, 1957) and by Gibson (1963) from their measurements of one-dimensional power spectrum, namely $\Lambda_f = \frac{1}{2}\pi[E_1(0)/\overline{u'^2}]$. This method requires extrapolation of the spectrum function to zero and is therefore only approximate. The present measurements were carried out to 0·5 Hz, and it appears (figure 8) that $E_1(n)$ remains constant at frequencies below 1 Hz. The calculated macroscale is $\Lambda_f/x = 0{\cdot}041$, which deviates by almost 7 % from the value obtained from the correlation measurements. An error of almost 100 % could occur, if the low frequencies were clipped at 3 Hz and a parabola fitted to the curve to obtain $E_1(0)$. This may indeed be the reason for the large discrepancies in Λ as shown in table 1.

The autocorrelation of the u' signal along the centre-line is plotted in figure 18. The abscissa on this figure is the time delay times the local mean velocity divided by x. As may have been expected, the autocorrelation function is self-preserving. The temporal integral scale obtained from this figure is $\Lambda_{f_T} = 0{\cdot}042x$, which is about 9 % larger than the macroscale obtained from the space correlations. Furthermore, Λ_{f_T} remains constant in the lateral direction as long as $y/x < 0{\cdot}1$, and then decreases rapidly (figure 19). This behaviour is contrary to expectation, since Λ_f obtained from the space correlations increases with y. Since the measurements were consistently repeatable, it appears that Taylor's hypothesis is not valid in this type of flow. Taylor's hypothesis is, in general, limited to uniform flow with low levels of turbulence; some criteria for the applicability of the

hypothesis in shear flow were given by Lin (1953). Accordingly, one may justify the application of the hypothesis if

$$\left|U\frac{\partial u'}{\partial x}\right| \gg \left|v'\frac{dU}{dy}\right| \quad \text{and} \quad \frac{\overline{u'^2}}{\overline{U}^2} \ll 1.$$

The first condition is satisfied, since

$$\frac{\overline{U}^2}{\overline{U}_m^2}\overline{\left(\frac{\partial u'}{\partial x}\right)^2} \Big/ \frac{\overline{v'^2}}{\overline{U}_m^2}\left(\frac{\partial \overline{U}}{\partial y}\right)^2 \approx 10^3,$$

but the second condition is violated almost everywhere in the flow, and particularly near the edges.

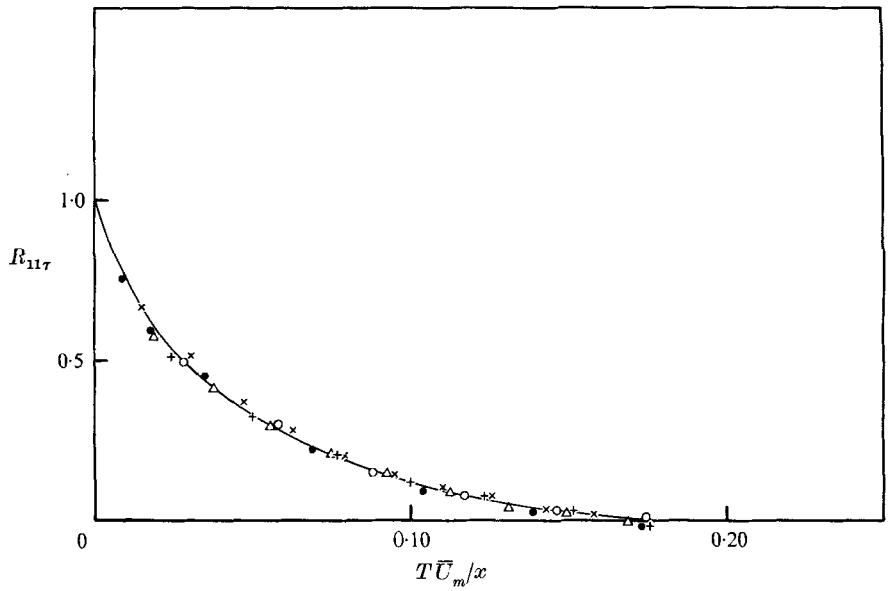

FIGURE 18. The autocorrelation of the u' signal along the jet centre-line. ●, x/D = 30; ○, 40; +, 60; ×, 75; △, 200. $\Lambda_{f\tau} = 0{\cdot}0420x$.

In view of the failure of Taylor's hypothesis in this flow, one must plot the autocorrelation results as a function of the average convection velocity of the energy-containing eddies. The convection velocity is obtained from the cross-correlation of the axial velocity fluctuation. One example of the plot of $R_{11\tau}$ is given in figure 20. From this figure one may construct curves of isocorrelations as a function of wire separation and time delay. Since the pattern of turbulence is not frozen, the definition of convection velocity is not unique, unless one obtains the correlations at a given frequency (see Wills 1964). Two average (representing all frequencies and averaged over time) convection velocities are conveniently defined from the cross-correlations, corresponding to the conditions

$$\left(\frac{\partial R}{\partial \delta}\right)_\tau = 0, \quad \left(\frac{\partial R}{\partial \tau}\right)_\delta = 0,$$

where δ is the separation between the hot wires and τ is the time delay. Drawing an envelope to the cross-correlation curves in figure 20, and taking the tangent

point to each curve of constant δ, yields the convection velocity $\langle \overline{U}_{c\tau} \rangle$ given by the first definition. Taking the time required for the maximum correlation for a given wire separation yields $\langle \overline{U}_{c\delta} \rangle$, corresponding to the second definition. The difference between the two varies from 10 to 20 %, depending on the location in the jet (figure 21). These results, however, are somewhat ambiguous, since the

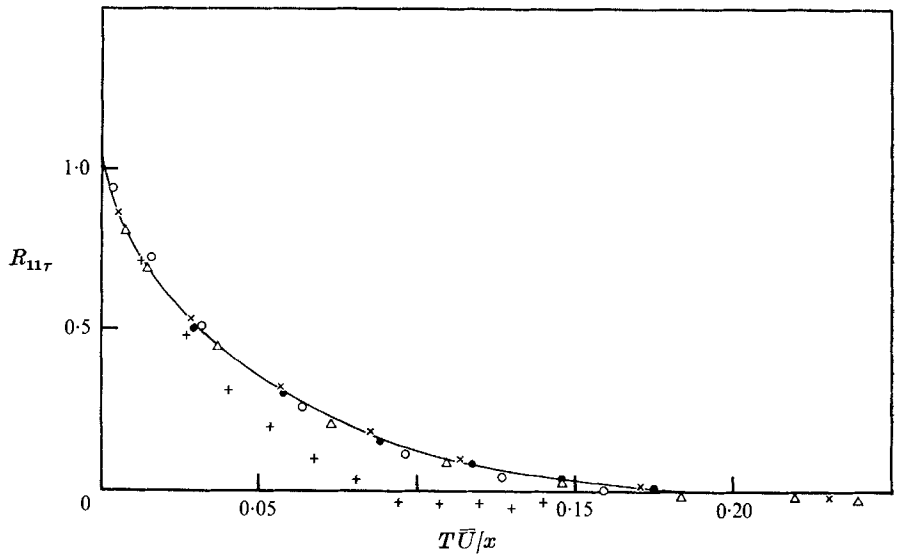

FIGURE 19. The lateral distribution of the autocorrelation of the u' signal. —, $\Lambda_{f\tau} = 0{\cdot}042x$, $x/D = 40$. ●, $y/x = 0$; △, 0·0121; ×, 0·05; ○, 0·097; +, 0·145.

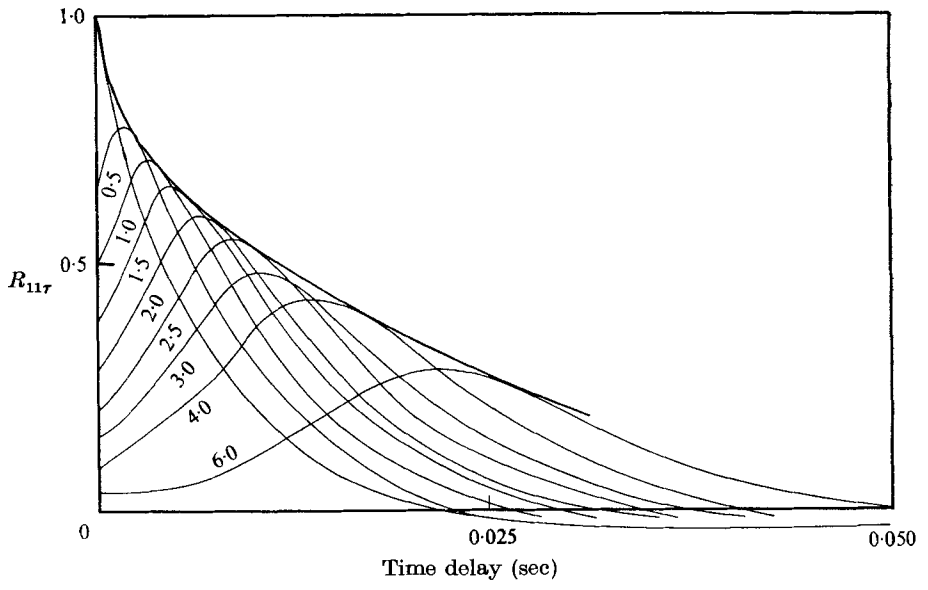

FIGURE 20. An example of the cross-correlation of the axial velocity fluctuations x/D, $y/x = 0{\cdot}012$. Curves represent downstream wire separation (in.), their envelope represents autocorrelation in the moving frame.

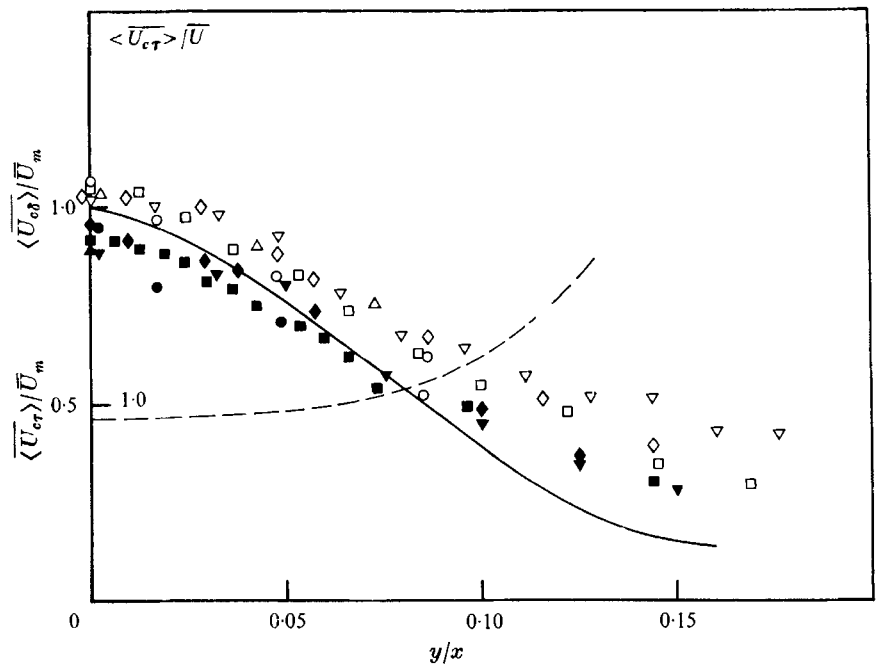

FIGURE 21. The distribution of convection velocity across the jet. $\langle \overline{U}_{c\tau}\rangle/\overline{U}_m$, $\langle \overline{U}_{c\delta}\rangle/\overline{U}_m$ (corresponding to $(\partial R/\partial\delta)_\tau = 0$, $(\partial R/\partial\tau)_\delta = 0$): ●, ○, $x/D = 30$; ■, □, 40; ◆, ◇, 50; ▼, ▽, 60; ▲, △, 70. — — —, $\langle \overline{U}_{c\tau}\rangle/\overline{U}$.

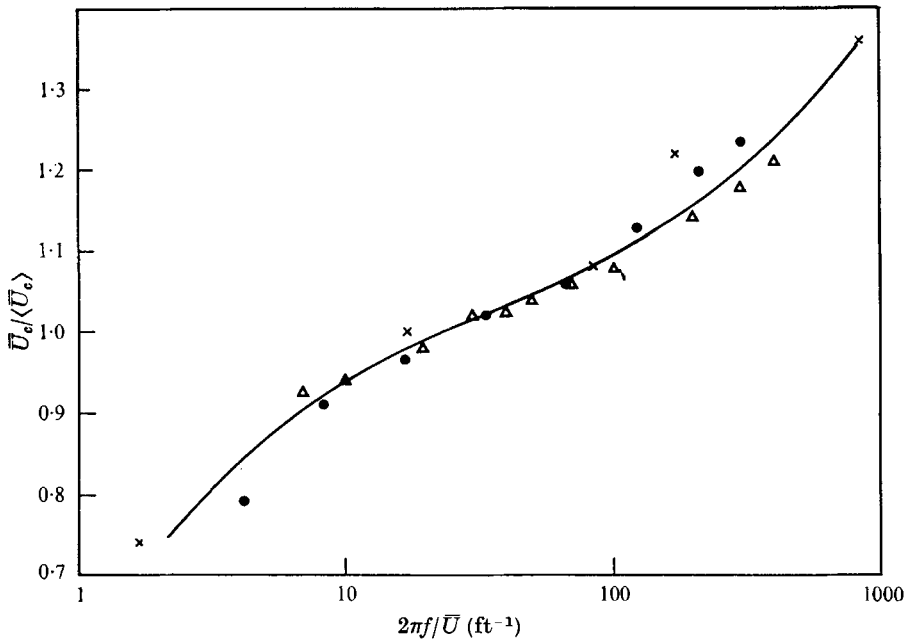

FIGURE 22. The dependence of the correlation velocity on the wave-number. △, Wills (1964) mixing layer; ●, present investigation, $x/D = 60$, $y/D = 0$; ×, present investigation, $x/D = 90$, $y/D = 0{\cdot}1$.

convection velocity, as defined above, is not entirely independent of the wire separation (Wills 1964). This effect may best be seen in figure 22, where the dependence of $\overline{U}_{c\tau}$ on the wave-number is shown. It appears that this dependence is the same for the jet as well as the mixing layer, since all points collapse approximately on one curve.

The fact that the small-scale motion is convected downstream faster than the large eddies across the entire width of the jet is quite puzzling. Another strange phenomenon is the relationship between the convection velocity and the mean velocity. Intuitively, one would expect the large-scale motion to be associated

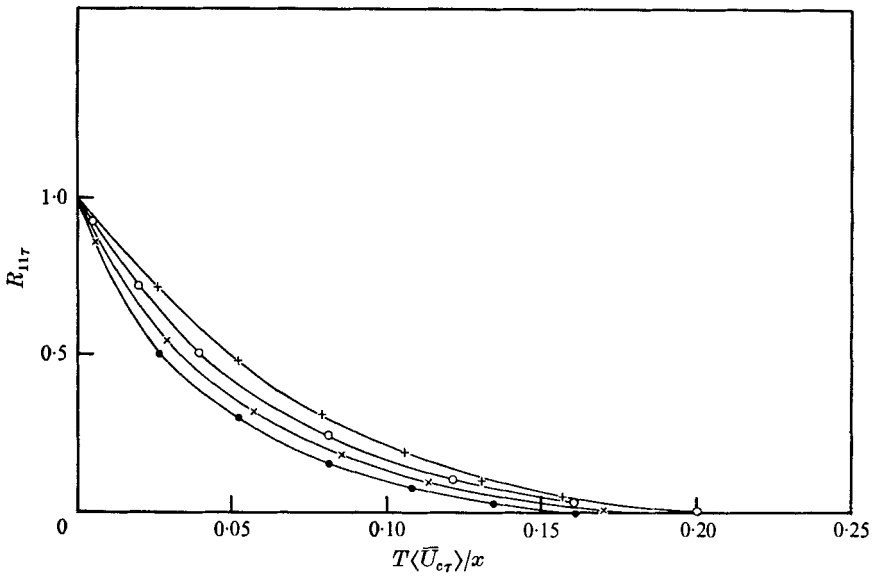

FIGURE 23. Lateral distribution of autocorrelations transformed with the convection velocity, ●, $\Lambda_{f\tau}/x = 0{\cdot}0387$, $y/x = 0$; ×, 0·043, 0·005; ○, 0·058, 0·097; +, 0·059, 0·145.

with the failure of Taylor's hypothesis in shear flow, and indeed at the centre-line of the jet this appears to be correct [$\langle\overline{U}_{c\tau}\rangle = \overline{U}_{c\tau}$ ($k \simeq 25$/ft.), and $\overline{U} = \overline{U}_{c\tau}$ ($k \simeq 90$/ft.)]. Towards the edge of the jet the situation is reversed, for example, at $\eta \equiv y/x = 0{\cdot}1$, $\overline{U} = \overline{U}_{c\tau}$ ($k \simeq 3{\cdot}5$/ft.). This effect can be explained only if there is also an appreciable convection velocity in the lateral direction.

The average convection velocity is now used to plot the lateral distribution of the autocorrelation measurements (figure 23). The agreement between the integral scales obtained in this manner and the ones obtained from the space correlations is much better. The scales increase with increasing η, as expected from figure 14. The discrepancy between the scales obtained in figure 14 and those in figure 23 is attributed to the use of an average convection velocity.

The envelope to the cross-correlation curves (figure 20) represents the autocorrelation in a frame moving with the average convection velocity $\langle\overline{U}_{c\tau}\rangle$. If the pattern of turbulence were frozen, this would have been a straight line given by $(R_{11\tau})_c = 1$; consequently, the deviation of this curve from unity represents the rate at which the velocity pattern is distorted. The variation of the moving-axis

autocorrelation along the axis of the jet is shown in figure 24; the self-preservation of this quantity is obvious from the figure. One may now define an integral time scale in the following manner:

$$(\Lambda_\tau)_c = \int_0^{T[(R_{11\tau})_c=\frac{1}{2}]} (R_{11\tau})_c \, dT.$$

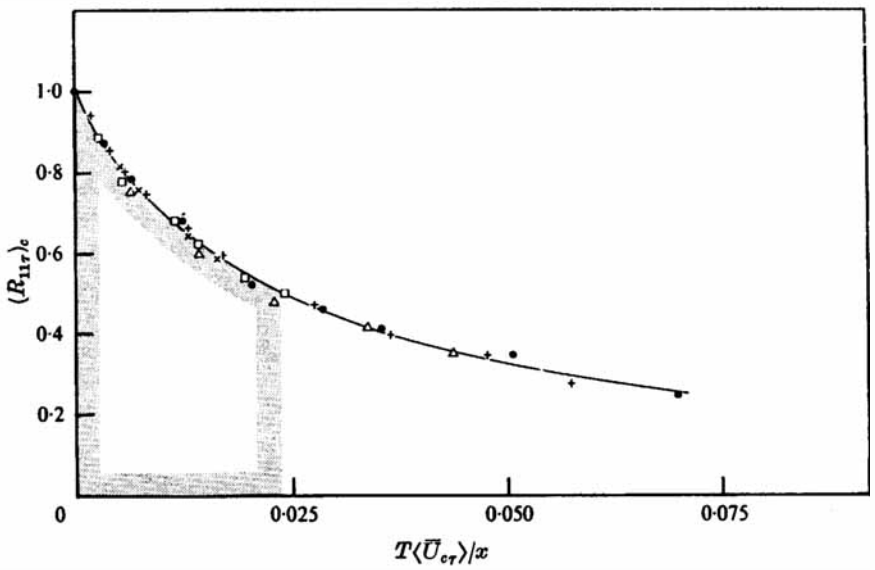

FIGURE 24. Variation of the moving-axis autocorrelation along the jet centre-line. ●, x/D = 20; +, 30; △, 40; □, 60; ×, 75. Shaded area, $(\Lambda_\tau)_c = 0{\cdot}0178x/\overline{U}_m$.

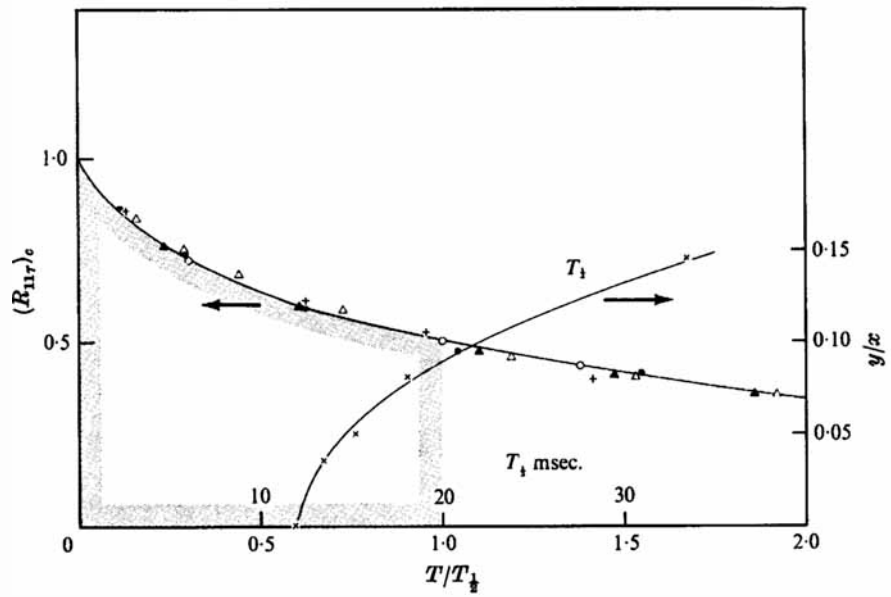

FIGURE 25. Lateral variation of the moving axis: integral time scale, $\eta = y/x$: ●, 0; △, 0·036; ○, 0·05; ▲, 0·097; +, 0·265. Shaded area, $(\Lambda_\tau)_c = 0{\cdot}668T_{\frac{1}{2}}$.

This definition is somewhat different from the customary one, in which the upper limit is taken as infinity, but the use of the present definition avoids the necessity for extrapolation. $(\Lambda_\tau)_c$ increases in the lateral direction in a similar manner to Λ_f (figure 25). The results in figure 25 collapsed on one curve by dividing the time delay by $T_{\frac{1}{2}}$, the time delay required for $(R_{11\tau})_c = \frac{1}{2}$.

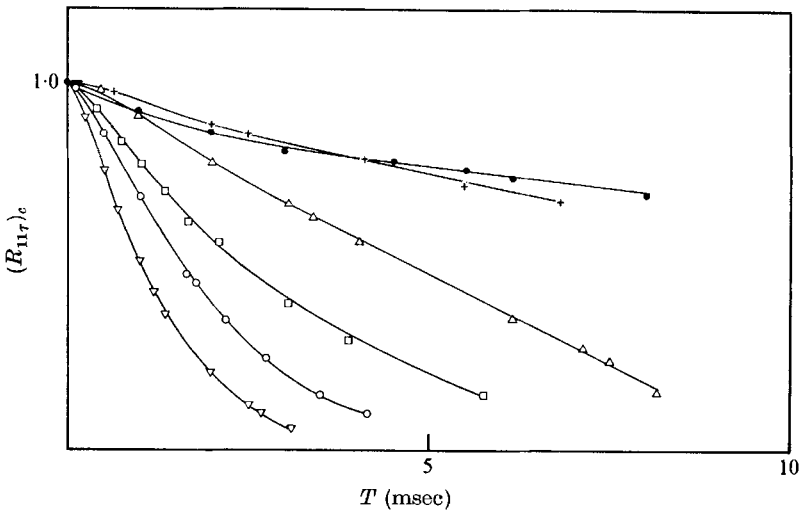

FIGURE 26. Dependence of moving-axis autocorrelation on frequency. ▽, 500 Hz; ○, 300; □, 160; △, 80; +, 40; ●, all frequencies.

In their investigation of the mixing region, Davies *et al.* (1963) observed that $(\Lambda_\tau)_c$ did not increase monotonically in the lateral direction. They have related this quantity to $(d\bar{U}/dy)^{-1}$, stating that it represents the production of turbulence from the mean shear. This is certainly not the case in the self-preserving jet, where $(\Lambda_\tau)_c$ increases monotonically outwards. Harmonic analysis of the cross-correlations indicates that the small-scale motion loses its identity faster than the larger-scale (figure 26), leading to the conclusion that $(\Lambda_\tau)_c$ is associated more closely with the dissipation term than the production.

7. The equations of the turbulent energy

The general form of the momentum equations in cylindrical co-ordinates is

$$\left.\begin{aligned}
&\frac{\partial U^2}{\partial x}+\frac{\partial UV}{\partial r}+\frac{1}{r}\frac{\partial UW}{\partial \phi}+\frac{UV}{r} = -\frac{1}{\rho}\frac{\partial \pi}{\partial x}+\nu\nabla^2 U,\\
&\frac{\partial UV}{\partial x}+\frac{\partial V^2}{\partial r}+\frac{1}{r}\frac{\partial VW}{\partial \phi}+\frac{V^2-W^2}{r} = -\frac{1}{\rho}\frac{\partial \pi}{\partial y}+\nu\left(\nabla^2 V-\frac{V}{r^2}-\frac{2}{r^2}\frac{\partial W}{\partial \phi}\right),\\
&\frac{\partial UW}{\partial x}+\frac{\partial VW}{\partial r}+\frac{1}{r}\frac{\partial W^2}{\partial \phi}+\frac{2VW}{r} = -\frac{1}{\rho r}\frac{\partial \pi}{\partial \phi}+\nu\left(\nabla^2 W-\frac{W}{r^2}+\frac{2}{r^2}\frac{\partial W}{\partial \phi}\right).
\end{aligned}\right\} \qquad (1)$$

Multiplication with U, V and W yields

$$\left.\begin{aligned}
&\frac{\partial U^3}{\partial x}+\frac{\partial U^2V}{\partial r}+\frac{1}{r}\frac{\partial U^2V}{\partial \phi}+\frac{U^2V}{r}=-\frac{2}{\rho}U\frac{\partial \pi}{\partial x}+2\nu\left[\tfrac{1}{2}\nabla^2U^2-\left(\frac{\partial U}{\partial x}\right)^2-\left(\frac{\partial U}{\partial r}\right)^2-\frac{1}{r^2}\frac{\partial U^2}{\partial \phi}\right],\\
&\frac{\partial UV^2}{\partial x}+\frac{\partial V^3}{\partial r}+\frac{1}{r}\frac{\partial V^2W}{\partial \phi}+\frac{V(V^2-2W^2)}{r}=-\frac{2}{\rho}V\frac{\partial \pi}{\partial r}+2\nu\left[\tfrac{1}{2}\nabla^2V^2-\left(\frac{\partial V}{\partial x}\right)^2-\left(\frac{\partial V}{\partial r}\right)^2\right.\\
&\qquad\left.-\frac{1}{r^2}\left(\frac{\partial V}{\partial \phi}\right)^2-\frac{V^2}{r^2}-\frac{2}{r^2}V\left(\frac{\partial W}{\partial \phi}\right)\right],\\
&\frac{\partial UW^2}{\partial x}+\frac{\partial VW^2}{\partial r}+\frac{1}{r}\frac{\partial W^3}{\partial \phi}+\frac{3VW^2}{r}=-\frac{2}{\rho}\frac{W}{r}\frac{\partial \pi}{\partial \phi}+2\nu\left[\tfrac{1}{2}\nabla^2W^2-\left(\frac{\partial W}{\partial x}\right)^2-\left(\frac{\partial W}{\partial r}\right)^2\right.\\
&\qquad\left.-\frac{1}{r^2}\left(\frac{\partial W}{\partial \phi}\right)^2-\frac{W^2}{r^2}+\frac{2}{r^2}W\left(\frac{\partial W}{\partial \phi}\right)\right].
\end{aligned}\right\}\tag{2}$$

The continuity equation in cylindrical co-ordinates is

$$\frac{1}{r}\frac{\partial}{\partial r}(rV)+\frac{1}{r}\frac{\partial}{\partial \phi}W+\frac{\partial}{\partial x}U=0.$$

Introducing $U=\overline{U}+u'$; $V=\overline{V}+v'$; $W=\overline{W}+w'$; $\pi=P+p'$

and (according to our co-ordinates)

$$x=x,\quad r=y\quad (r\phi=z=y\phi).$$

After some manipulation, averaging and adding yield

$$\left.\begin{aligned}
&\frac{\partial}{\partial x}[\overline{U}^3+\overline{V}^2\overline{U}+2\overline{V}\overline{u'v'}]+\frac{\partial}{\partial x}[3\overline{U}\overline{u'^2}+\overline{u'^3}+\overline{v'^2u'}+\overline{U}\overline{v'^2}+\overline{U}\overline{w'^2}+\overline{u'w'^2}]\\
&\quad+\frac{1}{y}\frac{\partial}{\partial y}y[\overline{v'u'^2}+\overline{v'w'^2}+\overline{v'^3}]+\frac{1}{y}\frac{\partial}{\partial y}y[\overline{U}^2\overline{V}+\overline{V}^3+\overline{V}\overline{u'^2}+\overline{V}\overline{w'^2}+3\overline{V}\overline{v'^2}+2\overline{U}\overline{u'v'}]\\
&\quad+\frac{2}{\rho}\left[\overline{U}\frac{\partial P}{\partial x}+\overline{V}\frac{\partial P}{\partial y}\right]+\frac{2}{\rho}\left[\overline{u'\frac{\partial p}{\partial x}}+\overline{v'\frac{\partial p}{\partial y}}+\overline{w'\frac{\partial p}{\partial z}}\right]\\
&=2\nu\left[\tfrac{1}{2}\nabla^2(\overline{u'^2}+\overline{v'^2}+\overline{w'^2})+\tfrac{1}{2}\nabla^2(\overline{U}^2+\overline{V}^2)-\overline{\left(\frac{\partial u'}{\partial x}\right)^2}-\overline{\left(\frac{\partial u'}{\partial y}\right)^2}-\overline{\left(\frac{\partial u'}{\partial z}\right)^2}\right.\\
&\quad-\overline{\left(\frac{\partial v'}{\partial x}\right)^2}-\overline{\left(\frac{\partial v'}{\partial y}\right)^2}-\overline{\left(\frac{\partial v'}{\partial z}\right)^2}-\overline{\left(\frac{\partial w'}{\partial x}\right)^2}-\overline{\left(\frac{\partial w'}{\partial y}\right)^2}-\overline{\left(\frac{\partial w'}{\partial z}\right)^2}-\overline{\left(\frac{\partial U}{\partial x}\right)^2}-\overline{\left(\frac{\partial U}{\partial y}\right)^2}\\
&\quad\left.-\overline{\left(\frac{\partial V}{\partial x}\right)^2}-\overline{\left(\frac{\partial V}{\partial y}\right)^2}-\frac{1}{y^2}(\overline{V}^2+\overline{v'^2}+\overline{w'^2})-\frac{2}{y}\overline{\left(v'\frac{\partial w'}{\partial z}-w'\frac{\partial w'}{\partial z}\right)}\right].
\end{aligned}\right\}\tag{3}$$

To obtain from this equation the energy equation for the turbulent motion alone, one must subtract the analogous equation for the mean flow. The energy relation for the mean flow is derived in the same way, and reads

$$\left.\begin{aligned}
&\frac{\partial}{\partial x}[\overline{U}^3+\overline{U}\,\overline{V}^2]+\frac{1}{y}\frac{\partial}{\partial y}[y(\overline{U}^2\overline{V}+\overline{V}^3)]+\frac{2}{\rho}\left[\overline{U}\frac{\partial P}{\partial x}+\overline{V}\frac{\partial P}{\partial y}\right]\\
&\quad=-2\frac{\partial}{\partial x}[\overline{U}\overline{u'^2}+\overline{V}\overline{u'v'}]+2\overline{u'^2}\frac{\partial \overline{U}}{\partial x}+\overline{u'v'}\frac{\partial \overline{V}}{\partial x}+\overline{v'^2}\frac{\partial \overline{V}}{\partial y}\\
&\qquad-\frac{1}{y}\frac{\partial}{\partial y}[y(2\overline{U}\overline{u'v'}+2\overline{V}\overline{v'^2})]-2\nu\left[\frac{\overline{V}^2}{y^2}-\overline{U}\,\nabla^2\overline{U}-\overline{V}\,\nabla^2\overline{V}\right].
\end{aligned}\right\}\tag{4}$$

Subtracting (4) from (3) and dropping certain terms which are obviously small (see also Laufer 1954), one obtains

$$\left.\begin{aligned}
&\underbrace{\frac{\partial}{\partial x}[\overline{U}(\overline{u'^2}+\overline{v'^2}+\overline{w'^2})]+\frac{1}{y}\frac{\partial}{\partial y}y[\overline{V}(\overline{u'^2}+\overline{v'^2}+\overline{w'^2})]}_{\text{Convection}}\\
&\underbrace{+\frac{\partial}{\partial x}[\overline{u'(u'^2+v'^2+w'^2)}]+\frac{1}{y}\frac{\partial}{\partial y}y[\overline{v'(u'^2+v'^2+w'^2)}]}_{\text{Diffusion}}\\
&\underbrace{+2\left[\overline{u'^2}\frac{\partial\overline{U}}{\partial x}+\overline{v'^2}\frac{\partial\overline{V}}{\partial y}+\overline{u'v'}\frac{\partial\overline{U}}{\partial y}\right]}_{\text{Production}}+\underbrace{\frac{2}{\rho}\left[\frac{\partial\overline{u'p}}{\partial x}+\frac{1}{y}\frac{\partial}{\partial y}(y\overline{v'p})\right]}_{\substack{\text{Pressure}\\ \text{transport}}}\\
&\underbrace{+2\nu\left[\overline{\left(\frac{\partial u'}{\partial x}\right)^2}+\overline{\left(\frac{\partial u'}{\partial y}\right)^2}+\overline{\left(\frac{\partial u'}{\partial z}\right)^2}+\overline{\left(\frac{\partial v'}{\partial x}\right)^2}+\overline{\left(\frac{\partial v'}{\partial y}\right)^2}+\overline{\left(\frac{\partial v'}{\partial z}\right)^2}\right.}_{\text{Dissipation}}\\
&\qquad\qquad\underbrace{\left.+\overline{\left(\frac{\partial w'}{\partial x}\right)^2}+\overline{\left(\frac{\partial w'}{\partial y}\right)^2}+\overline{\left(\frac{\partial w'}{\partial z}\right)^2}\right]}=0.
\end{aligned}\right\}\tag{5}$$

This form of the equation is essentially the same as the one given by Rouse (1960). To apply this balance to the self-preserving region of the jet, the equation is rendered dimensionless by introduction of the following parameters:

$$\eta = y/x, \quad R_D = U_0 D/\nu, \quad \overline{q^2} = \overline{u'^2}+\overline{v'^2}+\overline{w'^2}.$$

We further make use of the relation

$$\frac{\overline{U}_m}{U_0} \approx \frac{5{\cdot}4}{x/D}$$

(from figure 3), and divide by $\overline{U}_m^3$. The equation finally becomes

$$\left.\begin{aligned}
&\underbrace{\overbrace{-\frac{1}{2}\left[\eta\frac{\partial}{\partial\eta}\left(\frac{\overline{U}}{\overline{U}_m}\frac{\overline{q^2}}{\overline{U}_m^2}\right)+3\left(\frac{\overline{U}}{\overline{U}_m}\right)\left(\frac{\overline{q^2}}{\overline{U}_m^2}\right)\right]}^{A}+\overbrace{\frac{1}{2\eta}\frac{\partial}{\partial\eta}\left[\eta\left(\frac{\overline{V}}{\overline{U}_m}\right)\left(\frac{\overline{q^2}}{\overline{U}_m^2}\right)\right]}^{B}}_{\text{Convection}}\\
&\underbrace{-\frac{1}{2}\left[\overbrace{3\frac{\overline{u'q^2}}{\overline{U}_m^3}+\eta\frac{\partial}{\partial\eta}\left(\frac{\overline{u'q^2}}{\overline{U}_m^3}\right)}^{C}\right]+\overbrace{\frac{1}{2\eta}\frac{\partial}{\partial\eta}\left[\eta\frac{\overline{v'q^2}}{\overline{U}_m^3}\right]}^{D}}_{\text{Diffusion}}\\
&\underbrace{\overbrace{+\left(\frac{\overline{u'v'}}{\overline{U}_m^2}\right)\frac{\partial(\overline{U}/\overline{U}_m)}{\partial\eta}}^{E}+\overbrace{\left(\frac{\overline{v'^2}}{\overline{U}_m^2}\right)\frac{\partial(\overline{V}/\overline{U}_m)}{\partial\eta}}^{F}-\overbrace{\left(\frac{\overline{u'^2}}{\overline{U}_m^2}\right)\left[\left(\frac{\overline{U}}{\overline{U}_m}\right)+\eta\frac{\partial(\overline{U}/\overline{U}_m)}{\partial\eta}\right]}^{G}}_{\text{Production}}\\
&\underbrace{+\frac{1}{\rho}\left[\frac{1}{\eta}\frac{\partial}{\partial\eta}\left(\eta\frac{\overline{v'p}}{\overline{U}_m^3}\right)-\eta\frac{\partial(\overline{u'p}/\overline{U}_m^3)}{\partial\eta}-3\left(\frac{\overline{u'p}}{\overline{U}_m^3}\right)\right]}_{\text{Pressure transport } H}
\end{aligned}\right\}\tag{6}$$

$$+\underbrace{\frac{x^2}{5{\cdot}4R_{eD}\overline{U}_m^2}\left[\overline{\left(\frac{\partial u'}{\partial x}\right)^2}+\overline{\left(\frac{\partial u'}{\partial y}\right)^2}+\overline{\left(\frac{\partial u'}{\partial z}\right)^2}+\overline{\left(\frac{\partial v'}{\partial x}\right)^2}+\overline{\left(\frac{\partial v'}{\partial y}\right)^2}+\overline{\left(\frac{\partial v'}{\partial z}\right)^2}\right.}_{\text{Dissipation } I}$$

$$\left.\underbrace{+\overline{\left(\frac{\partial w'}{\partial x}\right)^2}+\overline{\left(\frac{\partial w'}{\partial y}\right)^2}+\overline{\left(\frac{\partial w'}{\partial z}\right)^2}\right]}=0.$$

8. The triple velocity correlations

Knowledge of the terms $\overline{u'^3}$; $\overline{u'v'^2}$; $\overline{u'w'^2}$; $\overline{v'^3}$; $\overline{v'u'^2}$; $\overline{u'w'^2}$ is necessary for evaluation of the diffusion parameters C and D in the energy equation. The values were measured at $x/D = 90$, and are presented in figure 27. The measurements were performed with an ordinary x-wire arrangement, where u' and v' or w' could be obtained simultaneously. The output of both hot-wire sets was then manipulated in the usual way with Philbrick equipment, and was integrated over a sufficient time. For the triple correlation of the two transverse velocity fluctuations $\overline{v'w'^2}$, the method described by Townsend (1949) was applied: the x-wire is placed in the flow in such a way that its plane is parallel to the flow and at an angle of $\beta = 45°$ to the y- and z-axes. The outputs of the hot-wire sets are then

$$E_1 \propto u' + k(v' + w'),$$

$$E_2 \propto u' - k(v' + w').$$

Subtraction of both signals gives

$$E_1 - E_2 \propto v' + w'.$$

The square of this combined signal yields

$$\overline{(E_1 - E_2)^2} \propto \overline{v'^2} + 2\overline{v'w'} + \overline{w'^2},$$

and the cube

$$\overline{(E_1 - E_2)^3} \propto \overline{v'^3} + 3\overline{v'^2w'} + 3\overline{v'w'^2} + \overline{w'^3}.$$

From symmetry about the y-axis: $\overline{w'^3}$, $\overline{v'w'}$ and $\overline{v'^2w'}$ vanish.

Then $$\overline{(E_1 - E_2)^2} \propto \overline{v'^2} + \overline{w'^2}$$

and $$\overline{(E_1 - E_2)^3} \propto \overline{v'^3} + 3\overline{v'w'^2},$$

and therefore the correlation

$$\frac{\overline{(E_1 - E_2)^3}}{[\overline{(E_1 - E_2)^2})]^{\frac{3}{2}}} = \frac{\overline{v'^3} + 3\overline{v'w'^2}}{(\overline{u'^2} + \overline{w'^2})^{\frac{3}{2}}},$$

from which $\overline{v'w'^2}$ was then evaluated.

The triple correlations can also be used for the correction of the non-linear hot-wire response. This correction has, however, not been applied to any of the measurements presented here.

The bulk convection as defined by Townsend (1949),

$$\frac{\overline{v'q^2}}{\overline{U}_m} = \frac{\overline{v'q^2}}{\overline{q^2}},$$

can be obtained from these values together with the turbulent intensities.

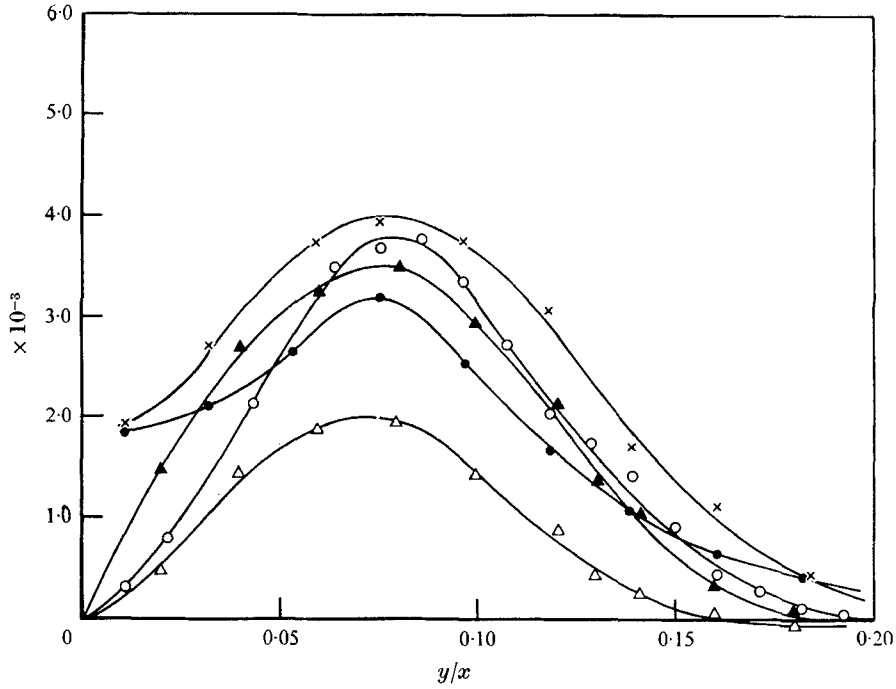

FIGURE 27. Distribution of triple correlation coefficients across the jet. ○, $\overline{v'u'^2}/\overline{U}_m^3$; ●, $\overline{u'w'^2}/\overline{U}_m^3$; ×, $\overline{u'v'^2}/\overline{U}_m^3$; △, $\overline{v'w'^2}/\overline{U}_m^3$; ▲, $\overline{v'^3}/\overline{U}_m^3$, $\overline{w'^3}/\overline{U}_m^3$.

9. The dissipation terms

The dissipation term in the energy equation is:

$$\Phi = \frac{x^2}{5{\cdot}4 R_{eD} \overline{U}_m^2}\left[\overline{\left(\frac{\partial u'}{\partial x}\right)^2} + \overline{\left(\frac{\partial u'}{\partial y}\right)^2} + \overline{\left(\frac{\partial u'}{\partial z}\right)^2} + \overline{\left(\frac{\partial v'}{\partial x}\right)^2} + \overline{\left(\frac{\partial v'}{\partial y}\right)^2} + \overline{\left(\frac{\partial v'}{\partial z}\right)^2} + \overline{\left(\frac{\partial w'}{\partial x}\right)^2} + \overline{\left(\frac{\partial w'}{\partial y}\right)^2} + \overline{\left(\frac{\partial w'}{\partial z}\right)^2}\right].$$

To obtain the nine spatial derivatives, two principal methods are available. (i) Approximation of the differential quotient by the difference quotient (Laufer 1954). (ii) Measurement of temporal derivatives and transformation to spatial derivatives in the flow direction by use of Taylor's hypothesis:

$$-\frac{\partial}{\partial x} = \frac{1}{\overline{U}}\frac{\partial}{\partial t},$$

where $\overline{U}$ is the mean velocity (Townsend 1947). The temporal derivatives of u', v' and w' have been obtained using ordinary electronic differentiation circuitry with a linear frequency dependence up to approximately 10 kHz.

In view of the shortcomings of Taylor's hypothesis in this kind of shear flow (this question has been treated earlier) the mean velocity $\overline{U}$ in the transformation from temporal to spatial derivatives is replaced by the convection velocity $\langle \overline{U^*_{c\tau}} \rangle$ of the $\partial u'/\partial t$ signal. This velocity essentially corresponds to the convection velocity of the small-scale motion. It was measured, whereupon it was found that $\langle \overline{U^*_{c\tau}} \rangle > \overline{U}$ at every point in the jet (figure 28). It was then assumed that

$$-\frac{\partial u'_{1;2;3}}{\partial x} = \frac{1}{\langle \overline{U^*_{c\tau}} \rangle} \frac{\partial u'_{1;2;3}}{\partial t}.$$

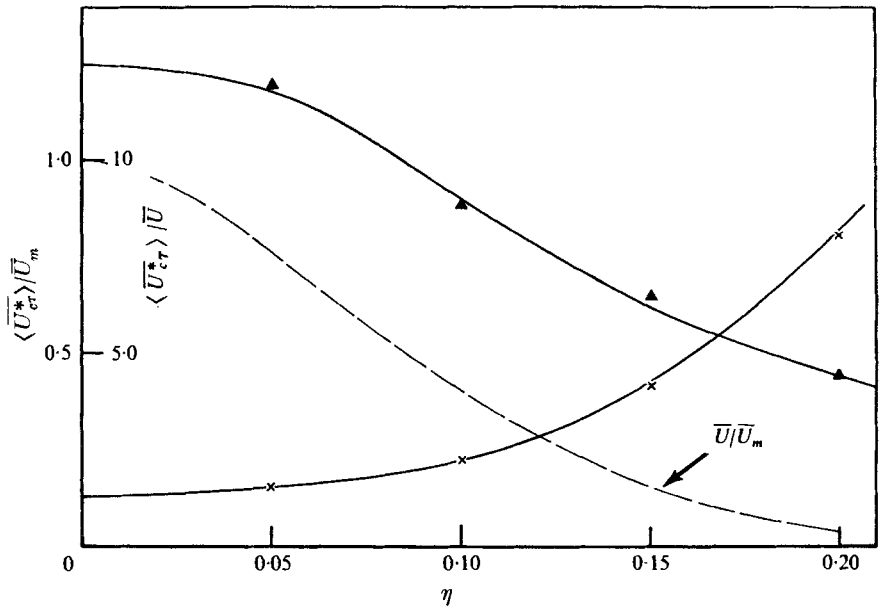

FIGURE 28. Distribution of the convection velocity of the dissipation scale across the jet. ▲, $\langle \overline{U^*_{c\tau}} \rangle / \overline{U}_m$; ×, $\langle \overline{U^*_{c\tau}} \rangle / \overline{U}$.

In figure 29 the values of

$$\frac{1}{\overline{U}_m^2}\left(\overline{\frac{\partial u'}{\partial x}}\right)^2, \quad \frac{1}{\overline{U}_m^2}\left(\overline{\frac{\partial v'}{\partial x}}\right)^2 \quad \text{and} \quad \frac{1}{\overline{U}_m^2}\left(\overline{\frac{\partial w'}{\partial x}}\right)^2$$

are plotted.

As for the lateral derivatives, only the approximate values could be measured by placing two hot wires very near together, so that by taking the r.m.s. value of the instantaneous difference of both signals the difference quotient was obtained (see also Laufer 1954). Only the values of

$$\frac{1}{\overline{U}_m^2}\left(\overline{\frac{\partial u'}{\partial y}}\right)^2 \quad \text{and} \quad \frac{1}{\overline{U}_m^2}\left(\overline{\frac{\partial u'}{\partial z}}\right)^2$$

were determined in this way as the necessity of a very small Δy or Δz eliminated the use of x-probes (figure 30).

These values were obtained with two hot wires of 1 mm length, placed at a distance of 0·25 mm. One must be extremely careful to match both (linearized)

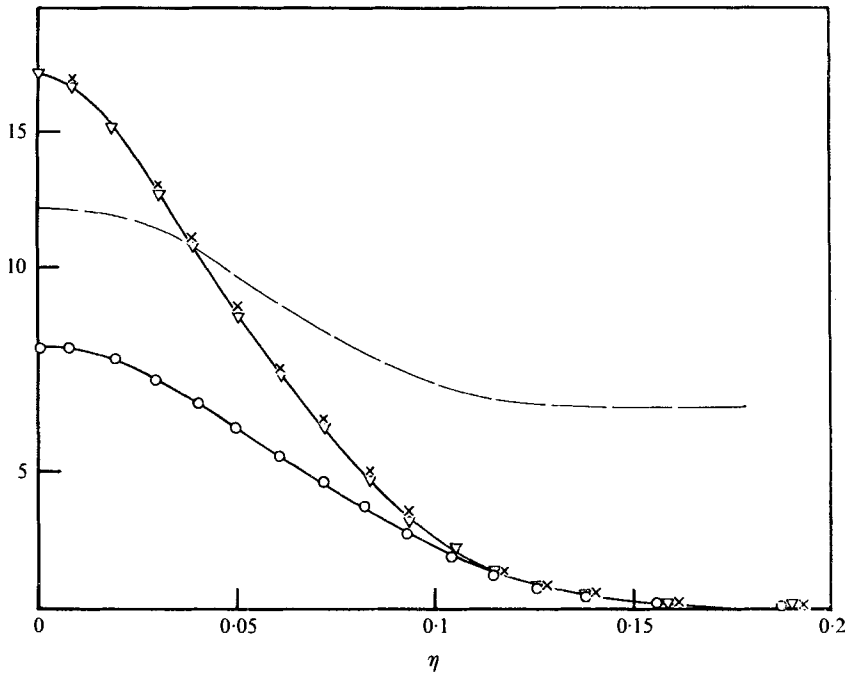

FIGURE 29. Distribution of dissipation terms:

$$---\left(\overline{\frac{\partial v'}{\partial x}}\right)^2 \Big/ \left(\overline{\frac{\partial u'}{\partial x}}\right)^2 = \left(\overline{\frac{\partial w'}{\partial x}}\right)^2 \Big/ \left(\overline{\frac{\partial u'}{\partial x}}\right)^2 = k \approx 1 + e^{-200\eta^2}$$

$$\text{O},\ \frac{x^2}{\overline{U}_m^2}\left(\overline{\frac{\partial u'}{\partial x}}\right)^2 \times 10^{-3};\ \nabla,\ \frac{x^2}{\overline{U}_m^2}\left(\overline{\frac{\partial v'}{\partial x}}\right)^2 \times 10^{-3};\ \times,\ \frac{x^2}{\overline{U}_m^2}\left(\overline{\frac{\partial w'}{\partial x}}\right)^2 \times 10^{-3}.$$

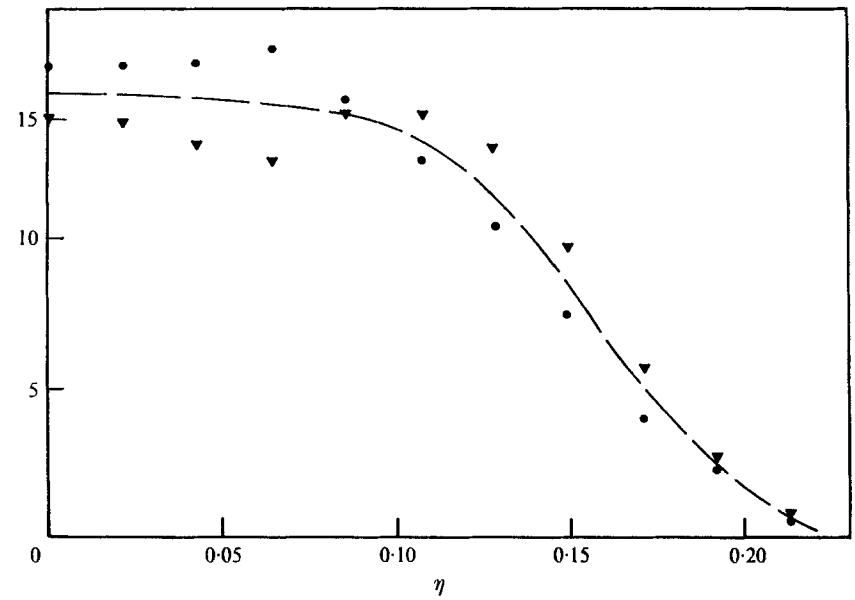

FIGURE 30. Distribution of dissipation terms:

$$\blacktriangledown,\ \frac{x^2}{\overline{U}_m^2}\left(\overline{\frac{\Delta u}{\Delta y}}\right)^2 \times 10^{-3};\quad \bullet,\ \frac{x^2}{\overline{U}_m^2}\left(\overline{\frac{\Delta u}{\Delta z}}\right)^2 \times 10^{-3}.$$

hot-wire outputs exactly; otherwise, low-frequency fluctuation of high intensity would not cancel out completely, and would therefore cause grossly erroneous readings. This is much more crucial in the intermittent region of a jet in still air than in most other flow configurations. As an additional safeguard, a filter was used which eliminated all frequencies of the $\Delta u'$-signal below 25 Hz. This value of 25 Hz is far below the energy-containing frequency of the time-differentiated signal, and thus has no influence on the true value itself.

The remaining four derivatives in the dissipation term must be inferred from isotropy considerations. It is assumed, in accordance with Laufer (1954) and Sami (1967), that isotropic relations hold for the mean square derivatives with respect to a given direction in the jet centre, but we note in addition (figure 29) a tendency towards anisotropy in the off-centre regions.

The relation

$$\overline{\left(\frac{\partial v'}{\partial x}\right)^2} = \overline{\left(\frac{\partial w'}{\partial x}\right)^2} \approx (1 + e^{-2\times 10^2 \times y^2}) \overline{\left(\frac{\partial u'}{\partial x}\right)^2}$$

describes this behaviour approximately. It is then assumed that

$$k\underline{\left(\frac{\partial u'}{\partial x}\right)^2} = \underline{\left(\frac{\partial v'}{\partial x}\right)^2} = \underline{\left(\frac{\partial w'}{\partial x}\right)^2},$$

$$\underline{\left(\frac{\partial u'}{\partial y}\right)^2} = k\underline{\left(\frac{\partial v'}{\partial y}\right)^2} = \underline{\left(\frac{\partial w'}{\partial y}\right)^2},$$

$$\underline{\left(\frac{\partial u'}{\partial z}\right)^2} = \underline{\left(\frac{\partial v'}{\partial z}\right)^2} = k\underline{\left(\frac{\partial w'}{\partial z}\right)^2},$$

where $k = 1 + e^{-2\times 10^2 \times y^2}$. The underlined terms denote the measured values. From figure 29 it is apparent that

$$\overline{\left(\frac{\partial u'}{\partial y}\right)^2} \approx \overline{\left(\frac{\partial u'}{\partial z}\right)^2}.$$

Hence, the dissipation term can be written in the following way:

$$\Phi = \frac{x^2}{5{\cdot}4\, R_{eD}\, \bar{U}_m^2}\left[\overline{\left(\frac{\partial u'}{\partial x}\right)^2} + 2\overline{\left(\frac{\partial u'}{\partial y}\right)^2}\left[2 + \frac{1}{1 + e^{-2\times 10^2 \times y^2}}\right] + 2\overline{\left(\frac{\partial v'}{\partial x}\right)^2}\right].$$

The variation of this 'semi-isotropic' term in brackets is plotted in figure 31, together with the isotropic value $15 \times \overline{(\partial u'/\partial x)^2}$ for comparison.

Clearly the isotropic concept does not hold over the entire jet region. Around the centre-line the isotropic value almost collapses with the 'semi-isotropic' one, but there is no real region of agreement. In fact, the distribution based on the assumption of isotropy falls very quickly below the 'semi-isotropic' distribution, and the integral values of both curves have a ratio of the order of two. Laufer (1954) reports for channel flow a factor of 2·5. This behaviour suggests an alignment of the small eddies with the mean flow direction. The dissipation term as calculated here is probably less accurate than the other terms needed for the energy balance. The experimental repeatability of the individual time derivatives was relatively poor, and in some cases the tendency towards isotropy

near the centre-line of the jet was not observed. The apparent anisotropy of the small-scale structure is currently under further investigation.

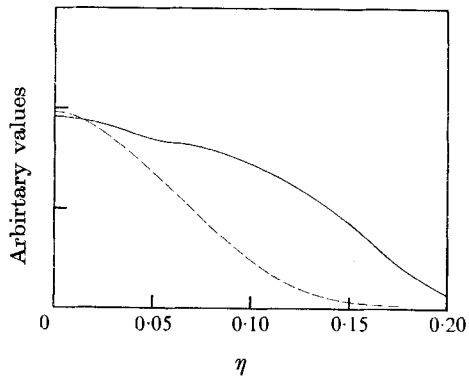

FIGURE 31. Comparison of complete dissipation term with isotropic distribution. ——, 'semi-isotropic'; – – –, isotropic.

10. The turbulent energy balance

From the measurements described earlier, all terms of the energy balance, with the exception of the pressure transport term H, were plotted, and H was obtained by difference. The detailed distribution is shown in figure 32. In figure 33 the turbulent energy balance is presented in the conventional way. The following observations can be made:

(i) The dissipation has a maximum on the jet centre-line. It is, however, almost constant in the inner region.

(ii) The production has a maximum at $\eta \approx 0{\cdot}052$ (maximum of shear stress at $\eta \approx 0{\cdot}058$), and is at this point approximately equal to the dissipation.

(iii) The convection is the largest contributor on the centre-line, where it has its maximum. It is there almost twice as large as the dissipation. At values $\eta > 0{\cdot}117$ the convection becomes negative.

(iv) The diffusion is largest at $\eta = 0{\cdot}030$, where it is of the same order of magnitude as the dissipation, the production and the convection.

(v) At $\eta \approx 0{\cdot}12$ the dissipation is balanced solely by production and diffusion.

(vi) The diffusion by pressure transport, which was obtained by difference, goes the same way as the diffusion by velocity fluctuations. It crosses the zero line at $\eta \approx 0{\cdot}12$, however.

Because of some uncertainties in the measurements, and the various differentiation processes involved in the evaluation of the energy terms, allowances with respect to accuracy have to be made. The accuracy of the balance can be assessed in part, however, from the requirement that the integral of the total lateral diffusion has to be zero. This check was performed; it may be observed in figure 34 that the area under the dashed line is approximately zero.

The overall picture of the energy balance is markedly different from the one obtained by Sami (1967). The measurements reported by Sami were made at a maximum distance of $x/D = 20$, where it is clearly shown that the state of

self-preservation is not yet reached, especially in case of higher-order or dissipation terms. It is believed, therefore, that the discrepancies observed result from the lack of self-preservation in Sami's (1967) measurements.

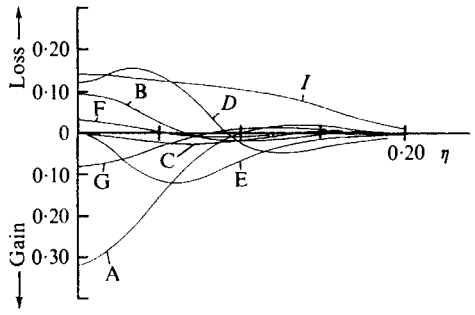

FIGURE 32

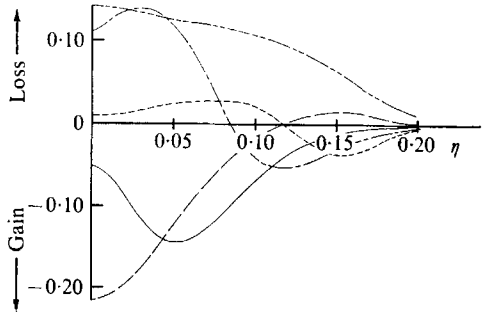

FIGURE 33

FIGURE 32. Detailed distribution of turbulent energy across the jet.

FIGURE 33. Turbulent energy balance (equation (6)). — · · —, dissipation; — · —, diffusion; — —, convection; ——, production; - - - -, pressure transport.

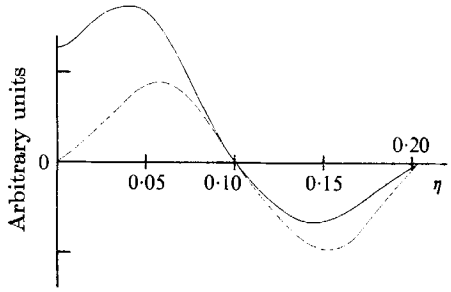

FIGURE 34. Distribution of the lateral diffusion. ——, total diffusion in y-direction; – – –, $\eta \times$ (total diffusion).

11. The turbulent microscales

The general definitions of the microscales λ_f and λ_g are (Hinze 1959)

$$\frac{1}{\lambda_f^2} = -\frac{1}{2}\left[\frac{\partial^2 f}{\partial(\Delta x)^2}\right]_{\Delta x=0} = \frac{1}{2\overline{u'^2}}\overline{\left(\frac{\partial u'}{\partial x}\right)^2},$$

and

$$\frac{1}{\lambda_g^2} = -\frac{1}{2}\left[\frac{\partial^2 g}{\partial(\Delta y)^2}\right]_{\Delta y=0} = \frac{1}{2\overline{u'^2}}\overline{\left(\frac{\partial u'}{\partial y}\right)^2}.$$

In addition to these conventionally used scales, we may define

$$\frac{1}{\lambda_g^{*2}} = \frac{1}{2\overline{v'^2}}\overline{\left(\frac{\partial v}{\partial x}\right)^2}.$$

From the spatial derivatives of the fluctuations described above, these scales can easily be computed.

Another method for measuring the microscale was proposed by Laufer (1948) and Liepmann (1949), based on a paper by Rice (1944, 1945). According to the analysis of Rice, the number of zero-passages per unit time, N_0, of a random, stationary signal u' is related to the signal derivative in the following way:

$$N_0 = \frac{1}{\pi}\left(\frac{\overline{\partial u'^2}}{\overline{\partial t}}\right)^{\frac{1}{2}} \Big/ (\overline{u'^2})^{\frac{1}{2}},$$

provided that both u' and $\partial u'/\partial t$ have a Gaussian probability-density distribution and $\overline{u'(\partial u'/\partial t)} = 0$. These two conditions, while being true for homogeneous

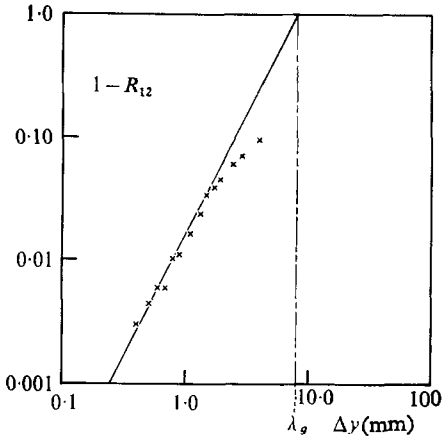

FIGURE 35. An example of the evaluation of microscale from lateral correlation.

turbulence, can only be approximately true in the centre of the jet, and will be violated in the off-centre regions. Measurements using this technique were nevertheless incorporated. A photomultiplier was used to count the zero passages of the signal on an oscilloscope screen. The measurements were made for the u' and the v' fluctuation along the jet centre-line, and across the jet at $x/D = 90$. The microscales were then computed from the formulae:

$$\lambda_f/\text{Count} = \frac{\langle \overline{U}_c^* \rangle \sqrt{2}}{\pi . N_{0u}},$$

and

$$\lambda_g^*/\text{Count} = \frac{\langle \overline{U}_c^* \rangle \sqrt{2}}{\pi . N_{0v}}.$$

Lastly, the scale λ_g was evaluated from the lateral correlation measurements, which are described in a previous section, and an example is shown in figure 35.

To obtain the microscales for the turbulent regions alone, one has to take the intermittency factor into account. On the centre-line $\gamma = 1$, and thus no correction is necessary. The variation of the microscales along the centre-line, as measured with the various methods, is given in figure 36.

It can be assumed that $\partial u_{1,2,3}/\partial t = 0$ in the irrotational region, and that $\langle \overline{U}_c^* \rangle$ is a convection velocity in the turbulent (i.e. rotational) régime only.

Thus, the results as obtained from the differentiated signal, and the convection velocity of the small scales represents approximately the microscale in the

rotational region. The microscales obtained from zero-counting have to be multiplied by γ to yield the values for the rotational regime. The lateral variation of λ_f, λ_g and λ_g^* for the rotational part of the jet, as obtained by the various

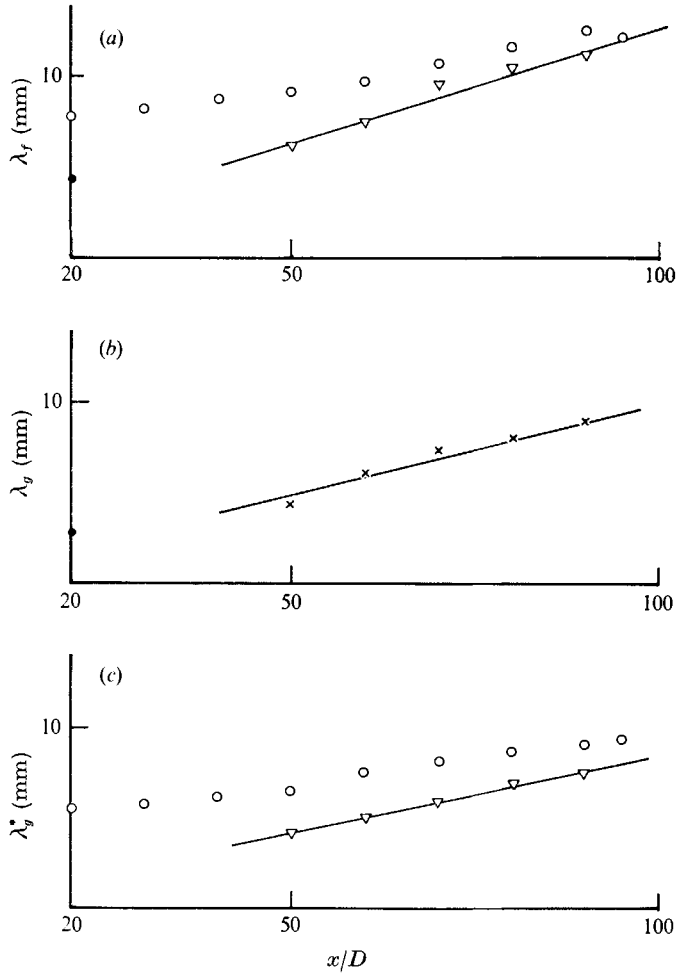

FIGURE 36. Variation of microscales along the jet centre-line. ●, Corrsin & Uberoi (1951); ○, from zero-counting; ▽, from differential signal; ×, from osculating parabola.

methods, is shown in figure 37. The measurements were taken at $x/D = 90$. The variations of the scales along the axis (figure 36) show self-preservation. The sizes of the scales are:

$$\lambda_f = 4{\cdot}8 \times 10^{-3} \times x,$$
$$\lambda_g = 3{\cdot}7 \times 10^{-3} \times x,$$
$$\lambda_g^* = 3{\cdot}2 \times 10^{-3} \times x.$$

The values obtained from zero-counting appear to be generally higher than those from the differentiated signal. This behaviour was also observed by Liepmann (1949) and Liepmann & Robinson (1953) and may probably be attributed to the

deviation of the turbulent fluctuation from the Gaussian probability distribution. The variation of the microscales across the jet, as presented in figure 37, shows a steep increase of λ_f towards the edges of the jet, whereas λ_g decreases, though to a lesser degree. The scale λ_g^* increases with η, as does λ_f, up to a value of

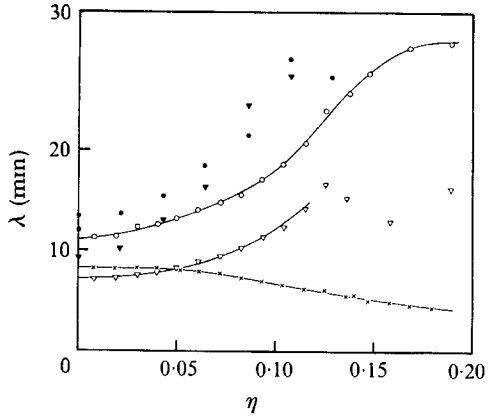

FIGURE 37. Variation of microscales across the jet.
●, ▼, zero-counting; ○, λ_f; ×, λ_g; ▽, λ_g^*.

approximately $\eta = 0{\cdot}12$. Since each of these scales depends on a different spectral function (E_1 or E_2), their similar dependence on η implies a similar relationship between the two one-dimensional spectra.

The values obtained by the zero-counting method are about 20 to 25 % larger than the ones measured with the differentiated signal on the centre-line. This discrepancy becomes more significant towards the outer regions. One can then conclude that the zero-counting method fails in this kind of flow.

12. Correction of microscales

The correction of the microscales resulting from a finite wire length is negligible. This may be shown for the case of λ_f.

The appropriate correction formula as given by Frenkiel (1954) is

$$\lambda_f^2 = \lambda_{f\,\mathrm{meas}}^2 \left[\frac{18 - G(l/\lambda)^2}{18 - 3(l/\lambda)^2}\right] = \lambda_{\mathrm{meas}}^2 k^2,$$

which is essentially equal to the formula used by Liepmann (1949). Then k is the correction factor, and the parameter G is defined, as in Batchelor & Townsend (1947), as

$$G = \overline{u'^2}\left(\overline{\frac{\partial^2 u'}{\partial t^2}}\right)^2 \Big/ \left[\left(\overline{\frac{\partial u'}{\partial t}}\right)^2\right]^2.$$

From measured energy spectra at $x/D = 90$ and $\eta \approx 0{\cdot}06$ it was found to be roughly equal to $G \approx 140$. With the hot-wire length $l = 1{\cdot}0$ mm and a measured $\lambda_f \approx 18$ mm, $(l/\lambda_f)^2 = 0{\cdot}0031$, and the correction factor becomes

$$k \approx 0{\cdot}985,$$

which is within the experimental scatter of the measurements.

As a matter of interest, it may be mentioned that the approximate relation $G = 0{\cdot}5R_{e\lambda_g}S$ (for $R_{e\lambda_g} \gg 1$), which is derived by Batchelor & Townsend (1947) for isotropic flow, yields a value of $G \approx 160$ (where S is the skewness factor).

13. Some comments about the properties of the turbulent fluid and the eddy structure

Some of the measurements may add to the information about the eddy structure in the jet, despite the fact that they are in no way comprehensive.

The one-dimensional spectra measured at two points in the flow (on the centre-line and at point of maximum shear) did not show a distinct two-component structure, as observed by Townsend (1950) in the self-preserving wake. About 50 % of the turbulent energy is associated with frequencies smaller than 5 Hz,

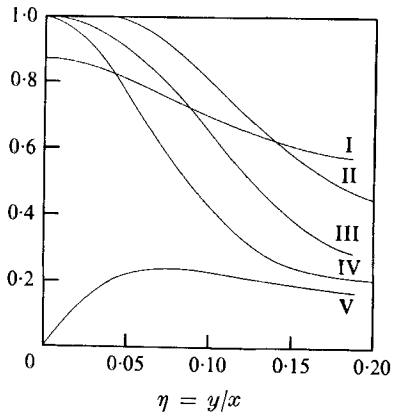

FIGURE 38. Lateral variation of some flow characteristics.

I, $\frac{\sqrt{v'^2}}{\sqrt{u'^2}}, \frac{\sqrt{w'^2}}{\sqrt{u'^2}}$; II, $\frac{\sqrt{(u'^2/\gamma)}}{\sqrt{u'^2_{c_L}}}$; III, $\frac{\sqrt{v'^2}}{\sqrt{v'^2_{c_L}}}, \frac{\sqrt{w'^2}}{\sqrt{w'^2_{c_L}}}$; IV, $\frac{\overline{U}}{\overline{U}_m\gamma}$; V, $\frac{\overline{u'v'}}{u'^2}$.

which would indicate that the energy-containing eddies are quite large. Indeed, the one-dimensional spectra peak at about 2 Hz. A loosely defined eddy, of a size equivalent to one-half of the jet-width, would correspond to a frequency of approximately 1 Hz. In this frequency range, the Koohn–Hite filter is best suited for spectral measurements, since it has a bandwidth equal to one half of the centre frequency. Thus, any discontinuity in the slope of the one-dimensional spectra (indicating a double structure) should be observed. It may also be noted that these large eddies carry most of the shear stress as well. This is in agreement with the measurements of Bradshaw *et al.* (1963) in the mixing region and the measurements of Bradbury (1965) in the two-dimensional jet; it is contrary to Townsend's large-eddy hypothesis.

As was already pointed out, the macro- and microscales of the eddies change quite significantly across the jet. The intensities in the turbulent fluid change somewhat less across the jet than the mean velocity, but the differences are not very significant (figure 38). The shear coefficient changes relatively little in the

outer part of the jet, yet it can hardly be considered a constant. The approximate mean value of $\overline{u'v'}/\overline{u'^2}$ over two-thirds of the jet width is 0·2, which is very much smaller than the corresponding value in the wake (Townsend 1956).

The eddy viscosity defined by

$$\frac{\overline{u'v'}}{\gamma\,\dfrac{\partial(\overline{U}/\gamma)}{\partial y}}$$

is constant across the flow, and the same is approximately true for the rate of energy dissipation within the turbulent fluid. This result is somewhat surprising, because the angle of strain, $\alpha_{\text{strain}} = \frac{1}{2}\tan^{-1}[\frac{1}{2}(d\overline{U}/\partial y)/(\partial\overline{U}/\partial x)]$, and the angle of stress, $\alpha_{\text{stress}} = \frac{1}{2}\tan^{-1}[2\overline{u'v'}/(\overline{u'^2}-\overline{v'^2})]$, are quite different (figure 39). From previous results (Corrsin 1957) it appeared that the disparity between those angles was associated with the failure of the simple gradient hypothesis.

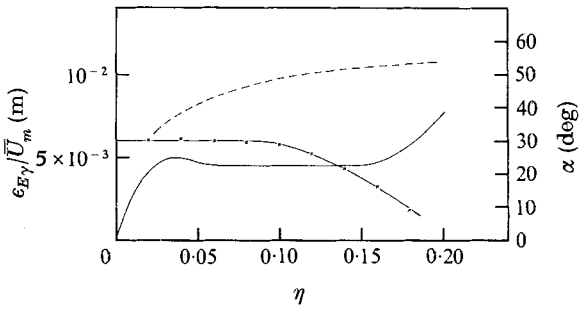

FIGURE 39. Lateral distribution of stress and strain angles and the turbulent energy diffusion coefficient. – – –, α strain; ——, α stress; —×—, $\epsilon_{E\gamma}/\overline{U}_m$.

From the triple correlations one can obtain the rate of transport of turbulent energy across the jet:

$$\overline{v'q^2} = \overline{v'u'^2} + \overline{v'^3} + \overline{v'w'^2}.$$

The energy diffusion coefficient ϵ_E may then be defined as

$$\epsilon_E = -\frac{\overline{v'q^2}}{\dfrac{\partial}{\partial\eta}(\overline{q^2})}.$$

Taking the intermittency into account, the relation for the rotational régime becomes approximately

$$\epsilon_{E\gamma} = -\frac{\overline{v'q^2}}{\gamma\dfrac{\partial}{\partial\eta}\left(\overline{q^2}\,\overline{\frac{1}{\gamma}}\right)}.$$

As shown in figure 39, $\epsilon_{E\gamma}$ is constant in the region $0 \leqslant \eta \leqslant 0{\cdot}10$, and decreases when $\eta > 0{\cdot}10$. The value of $\epsilon_{E\gamma}$ in the central part of the jet is

$$\frac{\epsilon_{E\gamma}}{\overline{U}_m} \approx 6\times10^{-3}\,(\text{m}).$$

The value for the momentum exchange coefficient (i.e. eddy viscosity) was found to be

$$\frac{\epsilon_{My}}{\overline{U}_m} \approx 2{\cdot}3 \times 10^{-3}\,(\mathrm{m}),$$

which is of the same order of magnitude as the energy diffusion coefficient.

Thus, it appears that for the turbulent jet the concept of gradient diffusion of the turbulent energy is justified to some extent.

The authors are indebted to Dr F. H. Champagne, who constructed the jet facility. The help of F. Lange in the assembly of some of the instrumentation and collection of data is greatly appreciated.

REFERENCES

Batchelor, G. K. & Townsend, A. A. 1947 *Proc. Roy. Soc.* A **190**, 534.
Bradbury, L. J. S. 1964 *Aero Quart.* **15**, 281.
Bradbury, L. J. S. 1965 *J. Fluid Mech.* **23**, 31.
Bradshaw, P., Ferriss, D. H. & Johnson, R. F. 1963 *NPL Aero. Report* no. 1054.
Champagne, F. H. & Sleicher, C. A. 1967 *J. Fluid Mech.* **28**, 177.
Corrsin, S. 1943 *NACA Wartime Report* no. 94.
Corrsin, S. 1957 *Nat. Acad. Sci., Naval Hydrodyn. Publ.* 515.
Corrsin, S. & Uberoi, M. S. 1949 *NACA TN* 1865.
Corrsin, S. & Uberoi, M. W. 1951 *NACA Report* 1040.
Corrsin, S. & Kistler, A. L. 1955 *NACA Report* 1244.
Davies, P. O. A. L., Fisher, M. J. & Barratt, M. J. 1963 *J. Fluid Mech.* **15**, 337.
Frenkiel, F. N. 1954 *Aero. Quart.* **5**, 1.
Gibson, M. M. 1963 *J. Fluid Mech.* **15**, 161.
Heskestad, G. 1963 Doctoral Dissertation, Department of Mechanics, The John Hopkins University.
Hinze, J. O. 1959 *Turbulence.* New York: McGraw-Hill.
Hinze, J. O. & Van der Hegge Zijnen 1949 *Appl. Sci. Res.* **1A**, 435.
Kibens, J. & Kovasznay, L. S. G. 1967 Divisional Meeting APS, Lehigh University.
Laufer, J. 1948 Ph.D. Thesis, California Institute of Technology.
Laufer, J. 1954 *NACA Report* 1174.
Laurence, J. C. 1956 *NACA Report* 1292.
Liepmann, H. W. 1949 *Helv. Phys. Acta* **2**, 119.
Liepmann, H. W. & Robinson, M. S. 1953 *NACA TN* 3037.
Lin, C. C. 1953 *Quart. Appl. Math.* **10**, 295.
Phillips, O. M. 1955 *Proc. Camb. Phil. Soc.* **51**, 270.
Rice, S. O. 1944 *Bell System Tech. J.* **23**, 82.
Rice, S. O. 1945 *Bell System Tech. J.* **24**, 46.
Rouse, H. 1960 *La Houille Blanche* no. 3, 4.
Sami, S. 1967 *J. Fluid Mech.* **29**, 81.
Schlichting, H. 1961 *Boundary Layer Theory.* New York: McGraw-Hill.
Stewart, R. W. 1956 *J. Fluid Mech.* **1**, 593.
Tollmien, W. 1926 *ZAMM* **6**, 1.
Townsend, A. A. 1950 *Phil. Mag.* **41**, 890.
Townsend, A. A. 1947 *Proc. Camb. Phil. Soc.* **43**, 560.
Townsend, A. A. 1959 *Proc. Roy. Soc.* A **197**, 124.
Townsend, A. A. 1956 *The Structure of Turbulent Shear Flow.* Cambridge University Press.
Wills, J. A. 1964 *J. Fluid Mech.* **20**, 417.